Fall 5-13-2016

Ferromagnetic Resonance Studies of Coupled Magnetic Systems

Daniel J. Adams
University of New Orleans, djadams1@uno.edu

Ferromagnetic Resonance Studies of Coupled Magnetic Systems

A Thesis

Submitted to the Graduate Faculty of the
University of New Orleans
in partial fulfillment of the
requirements for the degree of

Master of Science
in
Applied Physics

by

Daniel Adams

B.S. University of New Orleans, 2014

May, 2016

Acknowledgements

Thank you to my advisor, Dr. Leonard Spinu. Being a part of your research group for the last three years has been an extremely rewarding experience. For all of the opportunities, guidance, and education you have given me, both in experimental physics and in preparing me for the future, I am unceasingly grateful.

To the other members of my committee:
Dr. Malkinski, thank you for providing me with the theoretical understanding of electricity and magnetism necessary for this research.
Dr. Stokes, thank you for being the person I could go to with any immediate problem that arose while Dr. Spinu was in Washington, as well as for providing me with the understanding of quantum mechanics necessary for my work.

To my closest colleague and friend in research, Dr. Artur Maksymov, you were always teaching me the things I did not understand on my own and advancing my knowledge of the things I learned. Thank you for everything.

Thank you to everyone else in the physics department, AMRI, my friends, and especially my research group. Denny, Shankar, Ali, Nicolas, and Dr. Jose Vargas, my first instructors in experimental magnetism, thank you for helping me through.

I would like to thank AMRI's director, Dr. John Wiley, for the advice he has given me throughout my research experience here at UNO.

I would like to thank Dr. Ganping Ju and Dr. Erol Girt for providing the SAF samples which made this work possible.

I also acknowledge the financial support of the Performance and Accountability Assistantship.

More than anyone I thank my mother. I would have never gotten this far without you.

Table of Contents

Abstract

The high-frequency properties of coupled magnetic systems have been investigated using vector network analyzer ferromagnetic resonance (VNA-FMR) spectroscopy. Synthetic Antiferromagnetic (SAF) structures consist of two ferromagnetic layers separated by a non-magnetic spacer, coupled through the indirect exchange interaction. The ferromagnetic layers of our samples were composed of FeCoB separated by a layer of Ru. The thickness of Ru was varied in the range of 8 to 18 Å among the samples studied, thus providing different strengths of the coupling between the ferromagnetic layers. Antiferromagnetic coupling can be quickly identified by the major hysteresis loop (MHL).

A new way of displaying FMR data for these trilayer samples is presented which completely preserves the anisotropy effects while fully characterizing the angular dependence of FMR. The advantage of our representation is that the high-frequency data can be easily compared to the static switching behavior at any angle obtained through susceptibility measurements.

Ferromagnetic resonance; Coupled; Synthetic antiferromagnet; Magnetization switching

Introduction

The magnetic switching and microwave properties of synthetic antiferromagnet (SAF) structures are interesting topics of study due to their technological and fundamental importance. SAF are a trilayer structure and are *magnetically coupled* systems, which means the behavior of one of the magnetic layers is directly affected by the behavior of the other. Due to their shape anisotropy, thermal stability, and controllable coupling, these systems are often applied in giant magneto-resistance (GMR) devices found in magnetic random access memory (MRAM), for example [1]. Additionally, SAF structures may be found in recording media [2], hard disk read heads [3], and magnetic sensors [4]. These devices rely on the sensitivity of their components to the low magnetic fields produced near them.

Since the direction of magnetization in each layer in the SAF device is critical to device operation, the switching properties must be precisely known. Moreover, as the devices using SAF structures operate at increasingly high frequencies, there is a need to know and understand both the static and dynamic switching properties of SAF structures. The static and dynamic regimes of SAF are determined by the external magnetic excitations. Thus, for magnetic excitations with the frequency much smaller than the frequency of precession of magnetic moments in the presence of a magnetic field (typically in the GHz range) one has a static regime ($f << 10^9$ Hz), whereas a dynamic regime is present for magnetic field excitations with frequencies $f \geq 10^9$ Hz .

In this work we were interested in determining experimentally the switching properties of SAF coupled magnetic systems using a critical switching approach. The static switching critical curve was obtained using a tunnel diode oscillator (TDO) method operating in the MHz range [5].

The dynamic switching critical curve was obtained using the VNA-FMR with the SAF samples coupled with a coplanar waveguide (CPW). Until now, the high-frequency absorption for a coupled magnetic system has not been constructed in an angular-dependent, switching-field-like approach.

In this thesis, a dynamic critical curve is constructed for a series of coupled trilayer samples. Using this curve, information about the sample's anisotropy is available upon inspection, and one may immediately identify the points of resonant absorption for a given magnetic field strength, orientation, and frequency. We also show how these high-frequency curves evolve from the static switching curves.

An outline by chapters is as follows:

Chapter 1: *Overview of Magnetism*. The conceptual visualization of ferromagnetism and antiferromagnetism are introduced in this chapter, as are all of the relevant magnetic energy terms which appear throughout this thesis. The content includes an overview of different types of anisotropy and other types of magnetic energy, including the exchange energy which is a critical property of the samples studied in this work. This chapter also includes a description of basic magnetization processes of ferromagnetic materials. The Stoner-Wohlfarth model is introduced, as is the concept of ferromagnetic resonance (FMR).

Chapter 2: *Experimental Techniques*. This chapter describes in detail different types of magnetic measurement techniques, including the major hysteresis loop, reversible susceptibility experiments, and ferromagnetic resonance spectroscopy.

Chapter 3: *Experimental Results*. In this chapter, we introduce the samples under study in this work – four magnetically coupled systems, two of which are SAF. The static switching curves of the SAF samples are shown, which have been determined experimentally. Also

reported are the high-frequency characterizations of the coupled magnetic systems, including a new way of representing FMR data for this type of sample.

Chapter 4: *Discussion and Conclusion*. In the final chapter, we draw conclusions from our dynamic critical curves, and the link between magnetic susceptibility and FMR is explained. A completed dynamic analog to the static critical curve is presented.

Chapter 1: Overview of Magnetism

The purpose of this chapter is to provide a background of magnetism required to understand the topics contained within this thesis. We will first review types of magnetism. The quantum mechanical nature of magnetism will be explained, as will be the interaction processes between neighboring electrons, which, as we will see, can be either direct or indirect. In the direct exchange, the direction of an electron's spin is determined by its neighboring electron, whereas in the indirect exchange, the spins are coupled across a much larger distance.

We will also discuss the free energy contained in a magnetic system. The energy of a system is crucial in the explanation of experimental results of magnetization measurements. An important concept to keep in mind is that a magnetic system will achieve equilibrium by minimizing its free energy.

Finally, magnetization processes will be explained. Magnetization switching and the Stoner-Wohlfarth model are covered as well. This section will introduce a very important concept which is main subject matter of this thesis and that is the phenomenon of ferromagnetic resonance (FMR).

1.1 Ferromagnetism and Antiferromagnetism

1.1.1 Ferromagnetic Order

Magnetization originates from the spin of an electron. In a ferromagnetic material, the electron spins of neighboring atoms align parallel to each other in the direction of an applied magnetic field. The magnetic susceptibility χ relates the material's magnetization to the applied field to which it is subjected. χ for a ferromagnetic material can be several orders of magnitude larger than that of a paramagnetic material. Magnetic susceptibility, in general, takes the form

$$\chi = \frac{\mathbf{M}}{\mathbf{H}} \tag{1.1}$$

For most crystals, χ is not a scalar quantity but a tensor. It is also non-linear in the case of a ferromagnetic material. The non-linearity of χ can be seen in a graph of magnetization **M** vs applied field **H**, where it becomes apparent that **M** also depends on the material's magnetization history. For these reasons, χ is more accurately written as

$$\chi_{ij} = \frac{\partial \mathbf{M}_i}{\partial \mathbf{H}_j} \tag{1.2}$$

in which it describes the magnetization in the i^{th} direction from a change in the j^{th} direction of the applied field.

1.1.2 Antiferromagnetic Order

In the case of antiferromagnetism, energy is minimized when the electron spins are aligned antiparallel. These materials then have a zero net magnetic moment. Further explanations of these types of magnetism will follow in the next section when the direct exchange energy is discussed.

1.1.3 Magnetic Domains

Magnetic domains are regions of uniform magnetization within a material. Domains within a crystal are separated by a wall, which is not a rigid, single atomic layer partition, but rather a stack of atomic planes in which the spin direction gradually changes [6]. By reduction of the material into these smaller regions of net magnetization, the total energy is reduced.

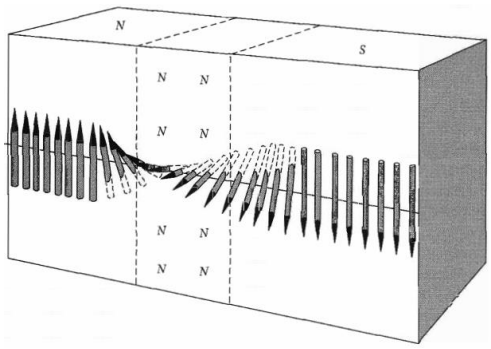

Fig. 1.1 Bloch wall (region between dotted lines) separating domains [6]

Microscopy methods which make a material's surface magnetization visible have been used to view magnetic domains. Magnetic force microscopy can be used to see magnetic domains even on the scale of a few nanometers. In a ferromagnetic material, domain magnetization will rotate to align parallel with a strong external magnetic field.

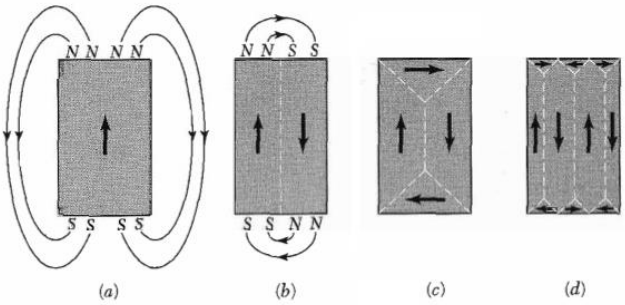

Fig. 1.2 The origin of domains [6]. (a) single domain resulting in a high value of magnetic energy. (b) magnetic energy is reduced by roughly one-half. (c) and (d) magnetic energy is zero

1.2 Magnetic Free Energy

1.2.1 Magnetocrystalline Anisotropy

Magnetic anisotropy refers to the directional dependence of magnetic properties, which can be observed by magnetic characterization measurements such as the major hysteresis loop (MHL) [7]. The directions which can be magnetized with the smallest applied field are referred to as the easy axes, and those that are a bit harder to magnetize are the hard axes. Anisotropy may be due to a material's shape, crystalline structure, stress, or may be induced by methods such as annealing.

Magnetocrystalline anisotropy is the only intrinsic form of anisotropy. The crystal anisotropy energy term has the same symmetry as the crystal structure itself. When a magnetic field **H** is applied, the electron orbital resists reorientation due to its coupling to the crystal lattice. Intrinsic anisotropy is the result of this coupling. It is this coupling which gives the material a preferred magnetization direction, along which the anisotropy energy is minimized.

In the case of cobalt, which exhibits *uniaxial* magnetocrystalline anisotropy, the easy axis is along the direction of the *c*-axis of its hexagonal crystal. The anisotropy energy is dependent on the angle θ of the magnetization vector **M** relative to the *c*-axis. Energy is minimized when $\theta = 0^o$ and increases with increasing θ. It is maximized when $\theta = 90^o$, when **M** is along the hard magnetization axis, and then decreases back to its original minimum value at $\theta = 180^o$ [8]. The uniaxial magnetocrystalline energy density is given by

$$E_k = K_0 + K_1 \sin^2\theta + K_2 \sin^4\theta + \ldots \qquad 1.3$$

where the coefficients K_n are the anisotropy constants with dimensions of energy per volume. K_0 is often disregarded since it is a constant. In this case of iron and nickel, the anisotropy constants are small, so the magnetocrystalline anisotropy is often considered negligible for these materials. For cobalt, on the other hand, K_1 is not small enough to disregard [9]. K_2 and higher-order coefficients are quite small, so the equation above is considered to be a good approximation.

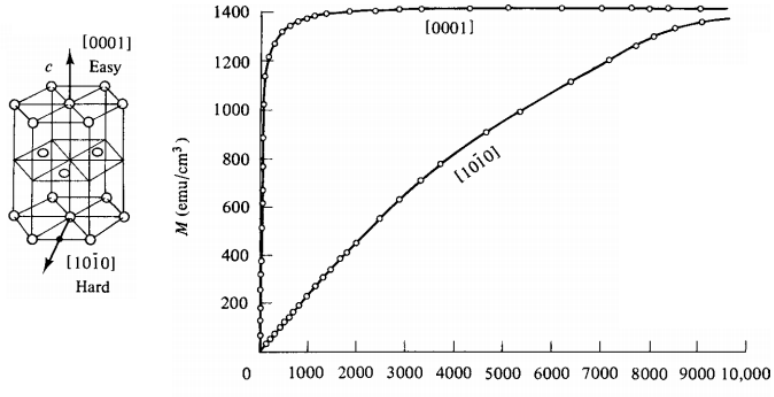

Fig. 1.3 The magnetocrystalline anisotropy of cobalt [7]. Left: Single crystal of cobalt with indicated magnetization axes. Right: Magnetization curves for a single crystal of cobalt. The higher curve corresponds to magnetization along the easy axis and the lower along the hard.

1.2.2 Shape Anisotropy

When a magnetic material is subject to an external applied magnetic field **H**, so-called free poles occur at the ends of the specimen, which produce a magnetic field that opposes the magnetization of the specimen. This is referred to as the demagnetizing field $\mathbf{H}_d$, such that

$$\mathbf{H}_d = -N\mathbf{M} \tag{1.4}$$

where **M** is the magnetization vector and N is the demagnetizing factor, which is dependent only on the shape of the specimen. A good example of a specimen with high shape anisotropy is a wire. Such objects with rod-like geometry exhibit a preferred magnetization along the long axis because the demagnetizing energy is smaller in this direction than along the transverse direction. This can be clearly seen in the magnetization curve of a magnetic nanowire.

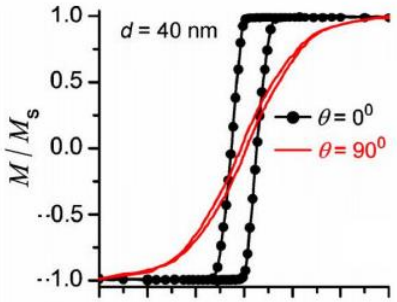

Fig. 1.4 Magnetization as a function of applied field for an array of nickel nanowires affected by shape anisotropy with the external field applied parallel (black) and perpendicular (red) to the wire axis [10].

1.2.3 Zeeman Energy

There is a potential energy associated with a polarized magnetic moment in a magnetic field. This interaction energy between the magnetization **M** and the external magnetic field **H** is called the Zeeman energy. It can be written as

$$E_Z = -\mathbf{M} \cdot \mathbf{H} \tag{1.5}$$

1.2.4 Exchange Energy

1.2.4.1 Direct Exchange

In 1928, Heisenberg developed the theory of quantum mechanical exchange interaction between magnetic moments in order to explain Weiss's phenomenological molecular field theory of ferromagnetism [8]. It is this exchange interaction, or spin-spin interaction, from which ferromagnetic behavior in materials develops. His theory suggested that if two electrons on neighboring atoms occupy the same orbital state, then by the Pauli exclusion principle their spins must align antiparallel to each other. If, however, the spins of the two electrons are parallel to one another, they must be in different orbital states [11]. This type of coupling in which electrons are close enough to have an overlap in their wavefunctions is called direct exchange.

The exchange energy is given by

$$E_{ex} = -2 \sum_{ij} J_{ij} \mathbf{S_i} \cdot \mathbf{S_j} \tag{1.6}$$

where $\mathbf{S_i}$ and $\mathbf{S_j}$ are the spin operators, and J_{ij} is the quantum mechanical exchange integral, which is indicative of the type of magnetism the material will display. For $J_{ij} > 0$, E_{ex} will be minimized when the spins align parallel to one another, meaning that the material will be ferromagnetic. Conversely, if $J_{ij} < 0$, E_{ex} will be minimized when the spins align antiparallel and the material will be antiferromagnetic.

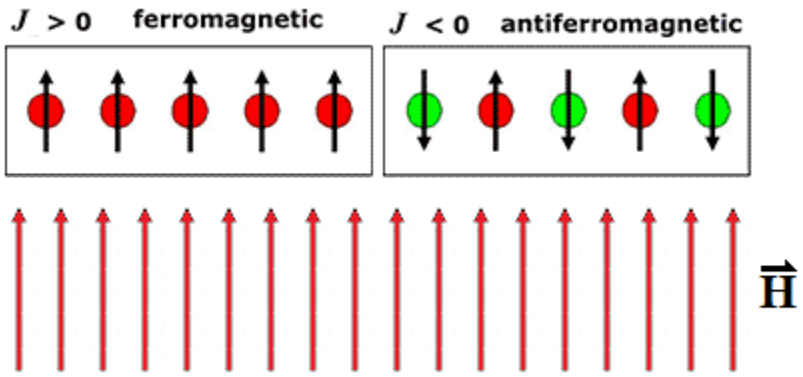

Fig. 1.5 Representation of spin orientation in ferromagnetism (left) and antiferromagnetism (right) with respect to an external applied magnetic field.

The coefficient J is, in general, difficult to evaluate. In 1933, it was found by Bethe that J is a function of interatomic spacing. It takes the form

$$J = \iint \psi_a^*(r_1)\psi_b^*(r_2)\left[\frac{1}{r_{ab}} - \frac{1}{r_{a2}} - \frac{1}{r_{b1}} + \frac{1}{r_{21}}\right]\psi_b(r_1)\psi_a(r_2)d\tau \qquad 1.7$$

where r_{21} is the distance between the electrons, r_{a2} and r_{b1} are the distances between the electrons and nuclei, and r_{ab} is the interatomic distance [12]. Values of r_{ab} as well as subshell radius r_d for various materials had been published by Slater three years earlier, in which he found that the ratio of these distances correlated with the sign of the exchange interaction [13, 14]. Slater's results helped in the evaluation of the J integral. The exchange integral can then be plotted as a function of the interatomic distance to obtain the now well-known Bethe-Slater curve [12]:

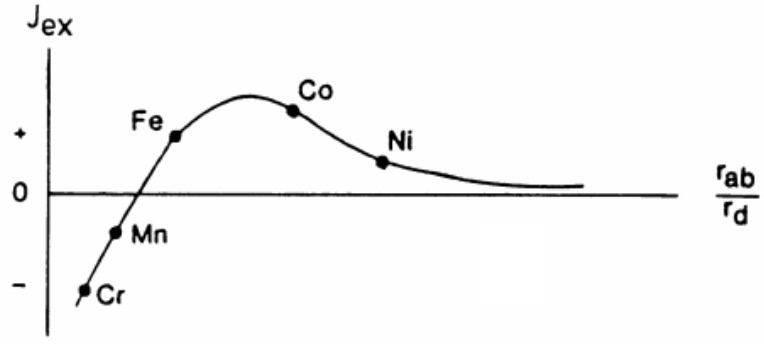

Fig. 1.6 Bethe-Slater curve

1.2.4.2 Indirect Exchange

When electrons are separated enough such that there is little to no overlap of their wavefunctions, they may be coupled through the *indirect* exchange, which is also called the Ruderman-Kittel-Kasuya-Yosida (RKKY) interaction [15]. Coupling of this type is mediated by the polarized conduction electrons. The idea of this interaction originated in 1954, when Ruderman and Kittel calculated the indirect exchange coupling of nuclear magnetic spins over long ranges [16]. They suggested that the spin density had an oscillatory behavior [17]. Their theory was expanded to electronic magnetic moments by Kasuya in 1956, who showed that the behavior displayed by the indirect exchange can be both ferromagnetic and antiferromagnetic [18], and Yosida in 1957 [19]. The coupling coefficient for the indirect exchange takes the form [15, 20]:

$$J_{ij}^{RKKY} = 9\pi \left(\frac{j^2}{\varepsilon_F}\right) F(2k_F r_{ij}) \tag{1.8}$$

where ε_F is the Fermi energy, k_F is the radius of the Fermi surface, r_{ij} is the distance between the point magnetic moments, and $F(x)$ is a function given by

$$F(x) = \frac{\sin x - x\cos x}{x^4} \tag{1.9}$$

$F(x)$ gives the coefficient an oscillatory behavior as a function of the separation between magnetic ions.

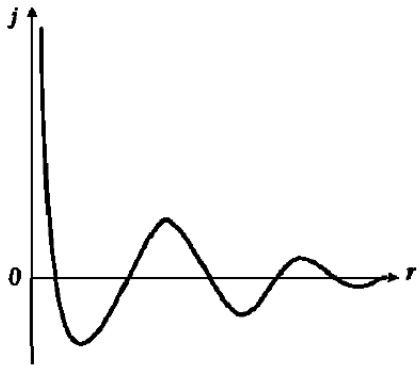

Fig. 1.7 Variation of the indirect exchange coupling coefficient *J* of a free electron gas in the neighborhood of a point magnetic moment at the origin, r = 0 [16].

1.3 Magnetization Processes

1.3.1 The Stoner-Wohlfarth Model

In 1948, Stoner and Wohlfarth attempted to explain the coercivity of a single-domain particle in a magnetic field by determining the energy as a function of the applied field **H** and angle θ of the magnetization vector [21] with the easy axis (see Fig. 1.8). The Stoner-Wohlfarth (SW) model, also called the coherent rotation model, is designed to predict the magnetic switching behavior of uniaxial monodomain ferromagnetic materials. The model assumes single-domain particles having uniform magnetization with constant magnitude throughout the particle. Such particles are also taken to be ellipsoidal, giving rise to the phenomenon of shape anisotropy. The magnetic moments do not move independently, but rather they move together, allowing the many magnetic moments to be considered as one large moment.

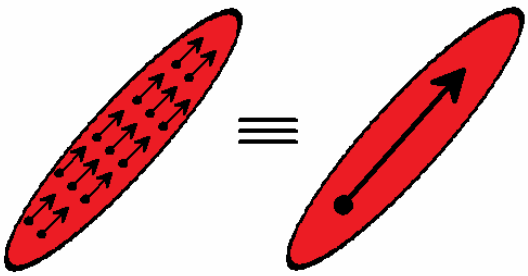

Fig. 1.8 An assembly of small magnetic moments considered as one large magnetic moment

The free energy of these so-called SW particles in an external magnetic field takes into account the anisotropy energy as well as the interaction with the external field.

$$E_T = E_k + E_Z \tag{1.10}$$

Substituting for anisotropy and Zeeman terms,

$$E_T = K_1 \sin^2\theta - \mathbf{M} \cdot \mathbf{H} \tag{1.11}$$

or, equivalently

$$E_T = K_1 \sin^2\theta - M_s H \cos(\theta - \theta_k) \tag{1.12}$$

where K_1 is the first-order anisotropy constant, M_s is the saturation magnetization, H is the magnitude of the applied field, and θ_k and θ are the angles between the easy axis and the normalized vectors $\mathbf{m} = \frac{\mathbf{M}}{M_S}$ and $\mathbf{h} = \frac{\mathbf{H}}{H_k}$ (where H_k is the anisotropy field)**,** respectively.

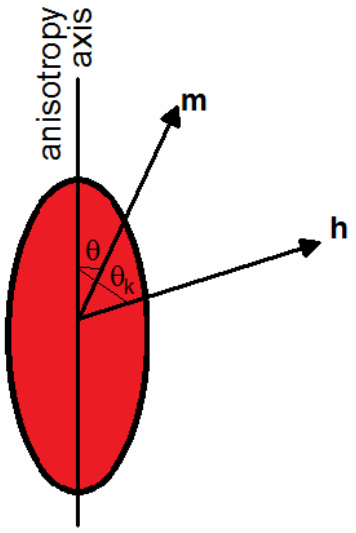

Fig. 1.9 SW particle with indicated anisotropy axis, **m**, and **h** vectors

The magnetic moment will orient itself such that the total energy is minimized, which may occur smoothly or abruptly, as in magnetization switching. This implies that there is a value for **H** where **M** is discontinuous and a magnetization switching occurs [22]. At equilibrium, the **M** vector will be defined by an angle θ^* at which the energy is minimum. Differentiating the

total energy with respect to θ and then differentiating a second time, we arrive at the equations by which we can find the critical switching fields. The conditions of minimum energy at θ* are

$$\left(\frac{\partial E_T}{\partial \theta}\right)_{\theta=\theta*} = 0 \text{ and } \left(\frac{\partial^2 E_T}{\partial \theta^2}\right)_{\theta=\theta*} \geq 0 \quad 1.13$$

The second of these is the condition for stable equilibrium. From the first condition we find that

$$[2K_1 \sin\theta \cos\theta - M_s H \sin(\theta - \theta_k)]_{\theta=\theta*} = 0 \quad 1.14$$

and from the second,

$$[2K_1 (\sin^2\theta - \cos^2\theta) + M_s H \cos(\theta - \theta_k)]_{\theta=\theta*} = 0 \quad 1.15$$

which can be written as

$$[2K_1 \cos 2\theta + M_s H \cos(\theta - \theta_k)]_{\theta=\theta*} = 0 \quad 1.16$$

The second derivative is set equal to zero because this is the point between stable (> 0) and unstable (< 0) equilibrium. These equations can be normalized by the saturation magnetization and anisotropy field to get

$$\begin{gathered}[\sin\theta \cos\theta - h \sin(\theta - \theta_k)]_{\theta=\theta*} = 0 \\ [\cos 2\theta + \cos(\theta - \theta_k)]_{\theta=\theta*} = 0\end{gathered} \quad 1.17$$

Simultaneous solutions of these equations [7]give us the critical field and critical angle at which the magnetization vector will switch.

$$h_C^2 = 1 - \frac{3}{4}\sin^2 2\theta_C \quad 1.18$$

$$\tan^3\theta_C = -\tan\theta_k \quad 1.19$$

The component of **M** along **H** is

$$m_{||} = \cos(\theta - \theta_k) \quad 1.20$$

and perpendicular to **H** is [22]

$$m_{\perp} = \sin(\theta - \theta_k) \quad 1.21$$

When θ_k = 0 (i.e., h is along the anisotropy axis), $\theta = 0, \frac{\pi}{2}$, and $m_\perp = 0$. Therefore, the hysteresis loop is square. When $\theta_k = \frac{\pi}{2}$, $\theta = \frac{\pi}{2}$ and $m_{||} = h$, showing no hysteresis.

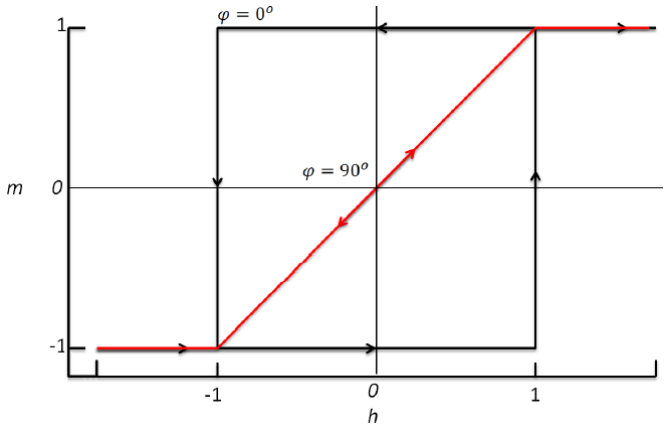

Fig. 1.10 Magnetization loops for a single-domain particle with **h** applied at 0° to the anisotropy axis (black) and 90° (red) [23].

The Stoner-Wohlfarth astroid (Fig. 1.11) – the critical curve for magnetization switching – is found as follows [7]. Starting with the anisotropy field,

$$H_k = \frac{2K_1}{M_s} \tag{1.22}$$

We define this equation in terms of its reduced components parallel ($h_{||}$) and perpendicular ($h_\perp$) to the easy axis.

$$h_{||} = \frac{H_{||}M_s}{2K_1} \text{ and } h_\perp = \frac{H_{||}M_s}{2K_1} \tag{1.23}$$

The total energy is now written taking both of these fields into account.

$$E_T = K_1 \sin^2\theta - H_{||}M_s \cos\theta - H_{||}M_s \sin\theta \tag{1.24}$$

We take the first derivative of the total energy in terms of the reduced components to find the equilibrium of magnetization and the second derivative to find the critical field.

$$\frac{\partial E_T}{\partial \theta} = \sin\theta\cos\theta + h_{||}\sin\theta - h_\perp\cos\theta = 0 \tag{1.25}$$

$$\frac{\partial^2 E_T}{\partial \theta^2} = \cos^2\theta - \sin^2\theta + h_{||}\cos\theta + h_{\perp}\sin\theta = 0 \quad (1.26)$$

Solving the above equations simultaneously, we arrive at solutions for $h_{||}$ and $h_{\perp}$.

$$h_{||} = -\cos^3\theta \text{ and } h_{\perp} = \sin^3\theta \quad (1.27)$$

These are the parametric equations that describe the astroid, which is defined as θ rotates from 0 to 2π.

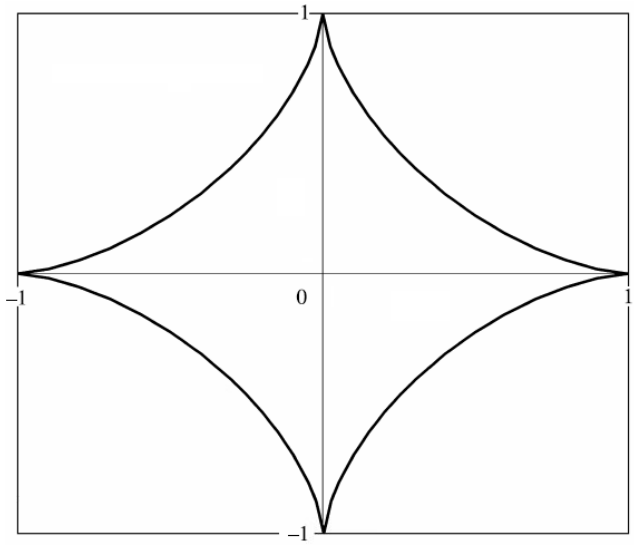

Fig. 1.11 The ideal switching astroid

This critical curve was developed to realize the points of stability in the magnetic system. The orientation of **m** for a given **h** can be found. When the critical curve is crossed during a field change, switching of **m** may occur, depending on its starting point.

1.3.2 Néel-Brown Model

Although the Stoner-Wohlfarth model is adequate to explain magnetization of non-interacting, single-domain particles with no thermal excitations, it fails in the case of thermal excitations. As the particle becomes thermally excited, the moments tend to decay exponentially toward thermal equilibrium [24]. The theory of thermal relaxation was first proposed by Néel [25] and developed further by Brown[26]. Both Néel and Brown derived a single relaxation time

under the assumption of an ideal particle. The Néel-Brown Model gives the relaxation time τ for the particle to spontaneously switch its magnetization by overcoming the anisotropy energy barrier.

$$\tau = \tau_0 e^{\frac{KV}{k_B T}} \tag{1.28}$$

where K is the anisotropy constant, V is the volume, k_B is the Boltzmann constant, and T is the temperature. The quantity $k_B T$ is the thermal energy and KV is the anisotropy energy barrier. The typical value for τ_0 is around 10^{-9} seconds.

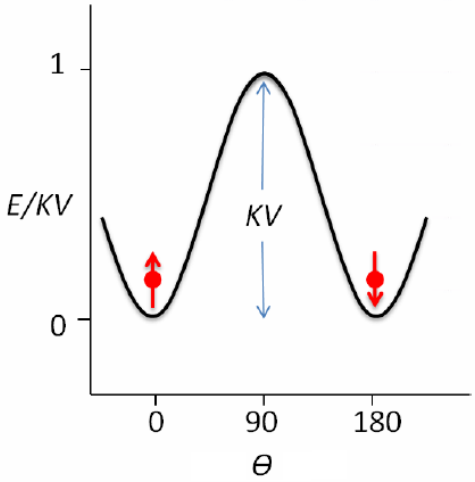

Fig. 1.12 Two equilibrium conditions separated by energy barrier KV

The magnetic behavior is dependent on the measurement time frame τ_m. If $\tau_m >> \tau$, the thermal relaxation is very fast and the energy barrier is easily overcome. In the case that $\tau_m << \tau$, then the relaxation time is slower and the system is stable.

1.3.3 Landau-Lifshitz-Gilbert Equation of Motion

In the previous sections, the process of magnetization switching was discussed without taking into account the time needed for the switching process to occur. When the time is taken into account, one needs to consider an equation of motion of the magnetization. When subjected to an external magnetic field, a magnetic moment **m** experiences a torque as it begins to align

with the field. In general, it will go into a precession, oscillating about the effective field direction. The motion of magnetization was originally described by Landau and Lifshitz. Recall the torque equation from mechanics

$$\mathbf{N} = \frac{d\mathbf{J}}{dt} = \mathbf{m} \times \mathbf{B} \tag{1.29}$$

and note that angular momentum **J** is proportional to the magnetic moment **m**, such that $\mathbf{m} = \frac{q_0}{2m_0}\mathbf{J}$, where $\frac{q_0}{m_0}$ is the charge-to-mass ration. Eq. 1.29 can now be rewritten as

$$\frac{d\mathbf{m}}{dt} = -\gamma(\mathbf{m} \times \mathbf{H}_{\text{eff}}) \tag{1.30}$$

where the constant term $\frac{q_0\mu_0}{2m_0}$ has been written as γ. This was adapted to a general equation which takes into account both precession *and* dissipation [27],

$$\frac{d\mathbf{m}}{dt} = -\gamma(\mathbf{m} \times \mathbf{H}_{\text{eff}}) - \frac{\lambda}{m^2}(\mathbf{m} \times \mathbf{m} \times \mathbf{H}_{\text{eff}}) \tag{1.31}$$

where λ in this case represents the relaxation frequency, which characterizes the dipole-dipole interactions between magnetic moments. The non-dimensional damping parameter $\alpha = \frac{\lambda}{\gamma m}$ may be introduced so that

$$\frac{d\mathbf{m}}{dt} = -\gamma(\mathbf{m} \times \mathbf{H}_{\text{eff}}) - \alpha\frac{\gamma}{M}(\mathbf{m} \times \mathbf{m} \times \mathbf{H}_{\text{eff}}) \tag{1.32}$$

This equation was modified by Gilbert in 1955 who replaced the damping term with a term which is dependent on the time derivative of the magnetic field.

$$\frac{d\mathbf{m}}{dt} = -\gamma^*(\mathbf{m} \times \mathbf{H}_{\text{eff}}) + \frac{\alpha_0}{M}\left(\mathbf{m} \times \frac{d\mathbf{m}}{dt}\right) \tag{1.33}$$

If $\alpha_0 = \alpha$ and $\gamma^* = \gamma(1 + \alpha_0^2)$ [28], then these equations may be written as

$$\frac{d\mathbf{m}}{dt} = -\gamma^*[\mathbf{m} \times (\mathbf{H} - \mathbf{H}_{\text{eff}})] \tag{1.34}$$

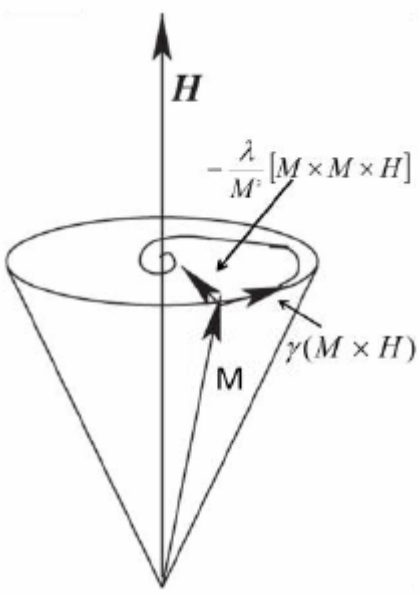

Fig. 1.13 Damped precession of the magnetic moment around the effective magnetic field.

1.3.4 Ferromagnetic Resonance

The phenomenon of ferromagnetic resonance (FMR) has advanced the study of ferromagnetic materials since 1948 when the number of papers published in this field increased dramatically and continued to rise. Researchers developed precise experimental techniques to study this resonant transfer of energy as theory continued to develop further.

The discovery is credited to Arkad'yev in 1911 when he noticed the absorption of radio frequency (rf) fields in ferromagnetic wires. The first quantum theory of the phenomenon was given by Dorfman [29] in 1923. This was followed by the theoretical analysis of ferromagnetic crystals in a variable magnetic field by Landau and Lifshitz in 1935 [30]. This theory was developed even further by Kittel [31] and Polder [32] in 1947 and 1949, respectively, and later by Gilbert [33] in 1955.

In the macroscopic description, when a magnetic material is subjected to a magnetic field, the magnetic moment **M** will precess around the direction of its local field, $\mathbf{H}_{\text{eff}}$, and eventually will be damped to align with $\mathbf{H}_{\text{eff}}$. If a transverse ac field, typically in the GHz range,

is introduced such that the ac frequency equals the frequency of precession, the resonance condition is satisfied, and there is an exchange of small energy quanta hv between the material and the electromagnetic radiation [28].

In the classical picture, although the ac magnetic field is oscillating with some angular frequency ω_0 in the plane perpendicular to $\mathbf{H}_{\text{eff}}$, when the resonance condition is satisfied the magnetic moment vector "sees" the ac field as constant, since its frequency of precession ω equals ω_0, and the resonant transfer of energy occurs [34]. **M** will begin to rotate in a wider path. With the tail of the vector remaining fixed, the vector will spiral to the opposite direction of its original orientation. This motion will continue until the resonance condition is no longer satisfied.

1.3.4.1 Mathematical Description of Resonance Condition

We will now show the mathematical description of the resonance frequency. For a thin film with uniaxial anisotropy, recall the energy terms (eqs. 1.3 – 1.6) for the total energy E. These equations are necessary to understand the total energy of the system. In the case of a single-layer thin film, the exchange interaction may be neglected. In spherical coordinates,

$$E = E(\theta, \emptyset) \tag{1.35}$$

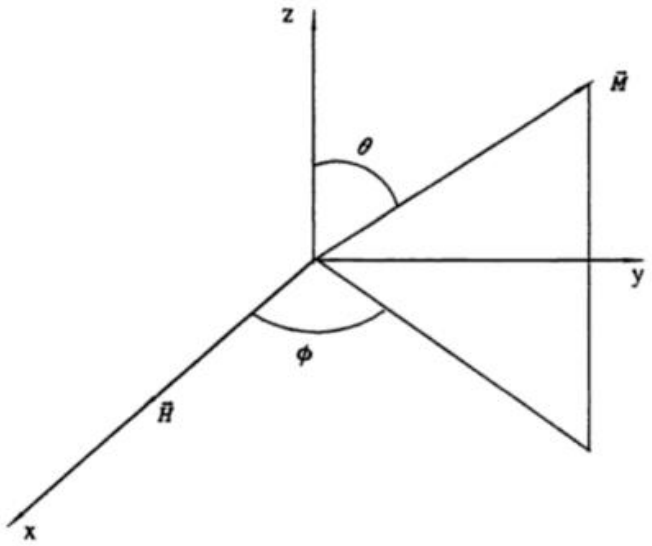

Fig. 1.14 Orientations of equilibrium magnetization **M** and the components of the dc external magnetic field **H** [35].

The angles of **M** are given by $(\theta, \emptyset)$ (see Fig. 1.14). We assume that **M**, and therefore *E*, are changing with time and that fluctuations in **M** are small. We express this as

$$\theta(t) = \theta_0(t) + \delta\theta$$
$$\emptyset(t) = \emptyset_0(t) + \delta\emptyset \qquad 1.36$$

Expanding *E* in a Taylor series,

$$E = E_0 + \frac{\partial E}{\partial \theta}\delta\theta + \frac{\partial E}{\partial \emptyset}\delta\emptyset + \frac{1}{2}\frac{\partial^2 E}{\partial \theta^2}\delta\theta^2 + \frac{1}{2}\frac{\partial^2 E}{\partial \emptyset^2}\delta\emptyset^2 + \frac{1}{2}\frac{\partial^2 E}{\partial\theta\partial\emptyset}\delta\theta\delta\emptyset + \cdots \qquad 1.37$$

and noting that at equilibrium, $\frac{\partial E}{\partial \theta} = \frac{\partial E}{\partial \emptyset} = 0$, so that energy can be written

$$E = E_0 + \frac{1}{2}\frac{\partial^2 E}{\partial \theta^2}\delta\theta^2 + \frac{1}{2}\frac{\partial^2 E}{\partial \emptyset^2}\delta\emptyset^2 + \frac{1}{2}\frac{\partial^2 E}{\partial\theta\partial\emptyset}\delta\theta\delta\emptyset + \cdots \qquad 1.38$$

The time dependence of the components of **M** can be found using eq. (1.30) ,

$$\frac{1}{\gamma}\frac{dM_\emptyset}{dt} = M_0 h_\theta$$
$$\frac{1}{\gamma}\frac{dM_\theta}{dt} = -M_0 h_\emptyset \qquad 1.39$$

where

$$M_\theta = M_0 \sin\theta_0 \delta\theta$$
$$M_\emptyset = M_0 \sin\theta_0 \delta\emptyset \quad (1.40)$$

and

$$h_\theta = -\frac{1}{M_0}(E_{\emptyset\theta}\delta\emptyset + E_{\theta\theta}\delta\theta)$$
$$h_\emptyset = -\frac{1}{M_0}(E_{\emptyset\emptyset}\delta\emptyset + E_{\emptyset\theta}\delta\theta) \quad (1.41)$$

Plugging these and the above values into eqs. 1.39

$$\frac{1}{\gamma}\frac{dM_\emptyset}{dt} = \frac{1}{\gamma}\frac{d}{dt}M_0 \sin\theta_0 \delta\phi = -(E_{\emptyset\theta}\delta\emptyset + E_{\theta\theta}\delta\theta)$$
$$\frac{1}{\gamma}\frac{dM_\theta}{dt} = \frac{1}{\gamma}\frac{d}{dt}M_0 \sin\theta_0 \delta\theta = (E_{\emptyset\emptyset}\delta\emptyset + E_{\emptyset\theta}\delta\theta) \quad (1.42)$$

Choosing $\delta\theta, \delta\emptyset \propto e^{i\omega t}$,

$$\frac{i\omega}{\gamma}M_0 \sin\theta_0 \delta\phi = -(E_{\emptyset\theta}\delta\emptyset + E_{\theta\theta}\delta\theta)$$
$$\frac{i\omega}{\gamma}M_0 \sin\theta_0 \delta\theta = (E_{\emptyset\emptyset}\delta\emptyset + E_{\emptyset\theta}\delta\theta) \quad (1.43)$$

each of which can be equated to zero so that the equations may be solved together.

$$0 = E_{\theta\theta}\delta\theta + (E_{\emptyset\theta} + \frac{i\omega}{\gamma}M_0 \sin\theta_0)\delta\phi$$
$$0 = E_{\emptyset\emptyset}\delta\emptyset + (E_{\emptyset\theta} - \frac{i\omega}{\gamma}M_0 \sin\theta_0)\delta\theta \quad (1.44)$$

Solving the determinant gives the classical condition for ferromagnetic resonance first derived by Smit and Beljers in 1954 [35].

$$\left(\frac{\omega}{\gamma}\right)^2 = \frac{1}{M_0^2 \sin^2\theta}\left(E_{\theta\theta}E_{\emptyset\emptyset} - E_{\emptyset\theta}^2\right) \quad (1.45)$$

Chapter 2: Experimental Techniques

2.1 Introduction: Static vs. Dynamic

The distinction between static and dynamic magnetization experiments has to do with the presence of an excitation magnetic field. A measurement such as susceptibility characterization is an example of a static experiment. In general, a static experiment involves an excitation frequency much lower than the frequency of precession, i.e., $f << 10^9$ Hz. Conversely, dynamic experiments require higher frequency excitation fields. In this type of experiment, there is competition between the two magnetic fields because the precessional frequency of a magnetic moment in a laboratory magnetic field is on the order of these angular frequencies.

2.2 Static Experimental Techniques

2.2.1 Major Hysteresis Loop (MHL)

The MHL is obtained using a vibrating sample magnetometer (VSM). The VSM is a highly sensitive susceptibility measurement system. A sample is suspended on a non-magnetic rod between a set of coils which produce a magnetic field. This field is constantly monitored by a built-in Hall effect gaussmeter. The sample is vibrated vertically at the midpoint of the magnetic field, centered in the small space between the signal pickup coils mounted on the poles of the magnet. Any resulting magnetic moment within the sample causes a proportional signal to be induced in these pickup coils. Signal processing ensures that the output signal is solely due to the magnetization of the material.

Alternatively to the VSM, an alternating gradient magnetometer (AGM) may be used to obtain the MHL. As with the VSM, a dc field is produced by a set of coils and constantly monitored by a gaussmeter, and the sample is magnetized by this field. However, rather than vibrating the sample, the AGM uses an alternating gradient field to produce a periodic force on

the sample. This gradient field interacts with the sample's magnetization, displacing the sample alternatively left and right, proportionally to its magnetic moment. A piezoelectric element which the sample rod is attached to measures the displacement. The system then outputs the measured magnetic moment of the sample as a function of applied field. The AGM is more sensitive than the VSM, able to measure magnetic moments in the range of nemu (10^{-9} emu), whereas the VSM is limited to moments on the order of μemu (10^{-6} emu).

The MHL is an incredibly useful characterization technique from which much useful information can be immediately identified by observation (see Fig. 2.1). Due to the usefulness and simplicity in obtaining, the MHL is often the first method used in magnetic material characterization. It is a ferromagnetic fingerprint of the material, containing information about the coercive field H_C (the field required to drive the magnetization of a material to zero), as well as the saturation magnetization and saturation field [36]. Often times the material will be completely saturated in the positive direction before taking data about the material's magnetization **M**. Data acquisition begins as the applied field **H** is decreased in regular increments. When **H** is reduced to zero, it is observed that the specimen still retains some positive magnetization. This is known as positive remanence [23]. As **H** continues decreasing into negative values, eventually reaching $\mathbf{H}_C$, **M** will become zero. As **H** becomes more negative, so will **M**, eventually reaching negative saturation. **H** is then increased from its most negative value, through zero, and back to its original positive state. The curve **M** vs. **H** this time takes a different path to return to its saturation magnetization. Thus, the MHL truly is a complete loop, containing information about the magnetization from both points of saturation.

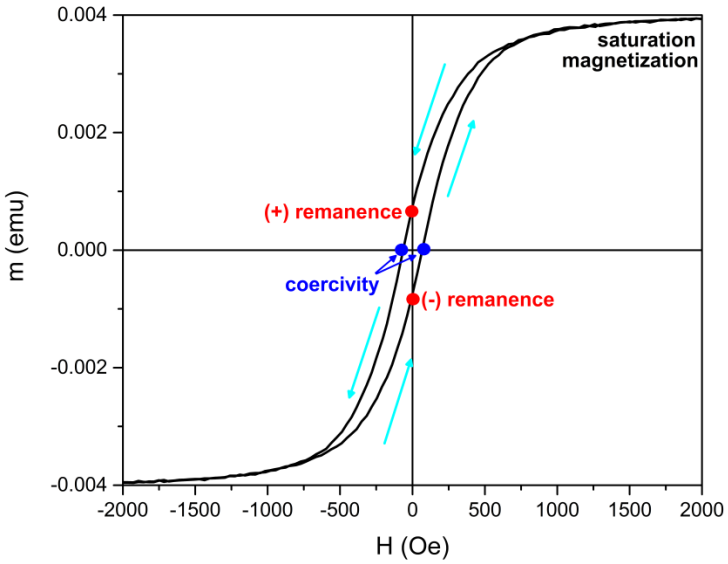

Fig. 2.1 MHL of a nickel nanostructure obtained by VSM. The blue arrows indicate the path direction of the loop.

2.2.2 Reversible Susceptibility Measurements

As seen in eq. 1.2, the susceptibility tensor χ_{ij} describes the change in a material's magnetization due to an incremental change in the applied field. If the change in the applied field provides only reversible change in magnetization we refer to the process as reversible susceptibility. In general this is the case for small magnetic field changes.

The transverse susceptibility (TS) of a material is a measure of the magnetic susceptibility in a direction transverse to an applied bias field, H_{DC} [20]. In 1909, TS was first discussed by Gans [37]. Nearly half a century later, Aharoni worked on the theory of TS and developed an expression for the TS tensor [38].

A measurement of a material's TS is performed using two magnetic fields: one dc magnetic field applied in any direction with respect to the easy axis, and an ac magnetic field applied perpendicular to the dc. From Aharoni's model, it was known that the TS signal would show sharp peaks when the dc field was equal to the sample's anisotropy field. This was considered to be a good technique for measuring anisotropy of particulate matter.

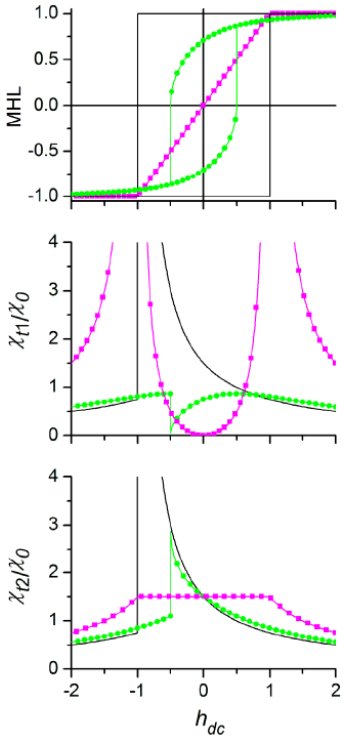

Fig. 2.2 MHL and TS for a single-domain particle for θ_k = 0º (black), 45º (green), and 90º(magenta). Recall from eq. 1.1 that the χ is magnetic susceptibility. $\chi_{t1} \equiv \chi_{xx}$ and $\chi_{t1} \equiv \chi_{yy}$ [39].

Fig. 2.2 shows the MHL and TS for a single-domain particle at different angles with respect to θ_k. From the top graph, one notices a discontinuity in the magnetization. For that same value of magnetic field, the TS measurements also show a discontinuity. It is suggested that the identification of anisotropy peaks offers a method for evaluating the sample's anisotropy [39].

In the case of a two-dimensional (2D) device, the switching characteristics are determined in the plane of the device. This allows one to determine the critical curve. The system's magnetic anisotropy determines the shape of the critical curve. As seen in the Stoner-Wohlfarth model [21], the critical curve for a single-domain particle with uniaxial anisotropy is an astroid. Although several methods have been introduced to determine the critical curve of 2D devices, the reversible susceptibility method has had much success [5, 40], as it is very general and can be applied to systems with any type of anisotropy.

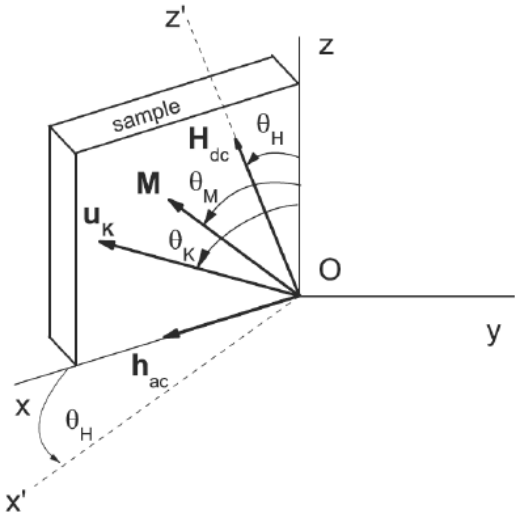

Fig. 2.3 Coordinate system of a 2D thin film

In 2006, Spinu [41] showed theoretically that TS is the zero-frequency limit of FMR, an idea which will be covered in a later chapter. The reversible TS in which the ac field frequency is small is given by

$$\chi_{xx} = \frac{M^2}{E_{\theta\theta}E_{\varphi\varphi} - E_{\theta\varphi}^2}\left[\sin^2\theta_M \sin^2\varphi_M E_{\theta\theta} + \frac{\sin 2\theta_M \sin 2\varphi_M}{2} E_{\theta\varphi} + \cos^2\theta_M \cos^2\varphi_M E_{\varphi\varphi}\right] \quad 2.1$$

where θ_M and φ_M are the equilibrium polar and azimuthal angles of **M**, and $E_{\theta\theta}$, $E_{\varphi\varphi}$, and $E_{\theta\varphi}$ are the second derivatives of the free energy density. This equation shows that TS can be used for probing the switching field since the denominator, $E_{\theta\theta}E_{\varphi\varphi} - E_{\theta\varphi}^2$, is the curvature of the free energy surface at equilibrium. The points for which the denominator is zero are the critical points of transition from one minimum to the other, i.e., the switching points.

The critical curve can be constructed by performing TS experiments at different angles in the plane of the sample. In this way, switching information is found at every angle at which the dc field is applied. The switching field is plotted as a point on a polar chart, and each of these is a point on the critical curve.

A slightly different approach keeps the sample fixed in place within the sensing coil (also fixed) and the dc field is rotated about this setup [5]. In this case, the susceptibility observed is

no longer TS, but rather is a combination of both transverse and longitudinal susceptibilities [40]. This combination still preserves the same singularities characterizing the switching fields.

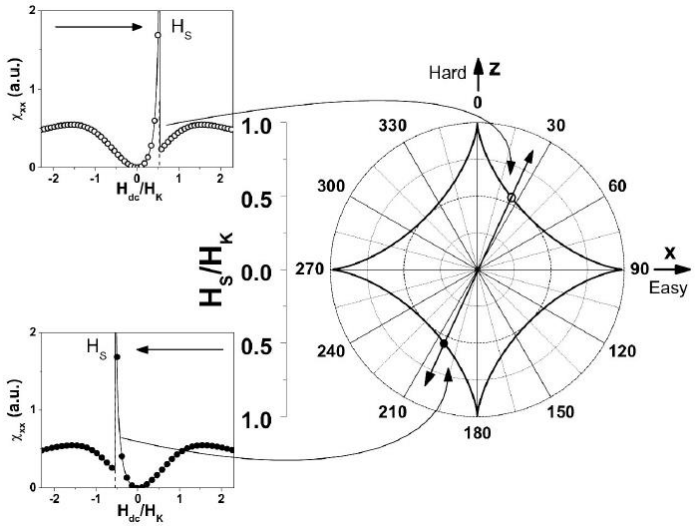

Fig. 2.4 *Left:* Susceptibility signal χ_{xx} for increasing (top) and decreasing (bottom) dc field sweeping at angle θ_H = 25º and θ_k = 90º. *Right:* Theoretical critical curve determined from susceptibility measurements for a uniaxial anisotropy system [5].

The latter approach can be easily achieved by the tunnel diode oscillator (TDO) method. A TDO is a self-resonating LC tank circuit driven by a tunnel diode, creating a highly sensitive method for detecting changes in magnetization. The TDO is well suited for operation in the radio frequency range [42]. The sample is placed inside the coil and a dc magnetic field is applied in the desired direction such that the ac field of the coil, external dc field, and anisotropy axis are all in the same plane. During the experiment, the dc field is applied at different angles to the sample's anisotropy axis. At every angle, the magnetic field is swept from positive saturation to negative. It has been shown [20] that the change detected in the TDO's resonant frequency is proportional to the change in the material's susceptibility.

$$\frac{\Delta f}{f} \propto \frac{\Delta \chi}{\chi} \qquad 2.2$$

2.3 Dynamic Experimental Techniques

2.3.1 Continuous Wave Ferromagnetic Resonance Spectroscopy

FMR is based on the absorption of electromagnetic radiation by the unpaired electrons. When scientists began to apply quantum mechanics to atoms, it was found that the atom has discrete energy levels. The energy differences studied through this technique are mainly due to the interaction of the unpaired electrons with an applied magnetic field. The electron will be in its lowest energy state when its magnetic moment is aligned with the applied field, and will be in its highest energy state when it is antiparallel to the field. As the magnetic field strength is increased, the energies of the two spin states diverge linearly. The electromagnetic radiation will be absorbed when the energy of the radiation equals the energy difference of the two spin states.

$$\Delta E = h\upsilon \qquad 2.3$$

It was noted [34] that for magnetic fields achievable in the laboratory, this absorption should occur in the microwave frequencies. Since its discovery in 1944 by Zavoisky [43], FMR has been applied in many areas of chemistry, physics, and materials science.

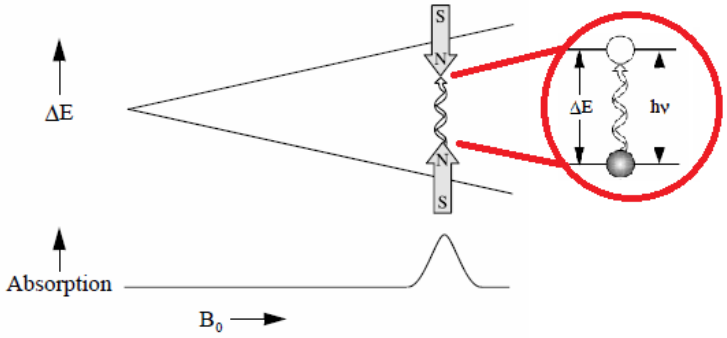

Fig. 2.5 Splitting of spin states with increased magnetic field

The Bruker spectrometer setup consists of a monochromatic microwave source, a waveguide, a resonator cavity, and a detector. These options may be changed to match the desired frequency (X-band or Q-band). The frequency of the source is tuned to the frequency of the cavity to minimize losses. The coils which create the magnetic field are external to the

cavity. The magnetic field is swept with the microwave frequency held constant. At resonance, the detector senses a minimum return of microwave energy. The output signal is the first derivative of the absorption, so it can typically be fitted using a Lorentzian derivative function.

2.3.2 Broadband Ferromagnetic Resonance Spectroscopy

While the X-band spectrometer is used for absorption measurements at some particular frequency, there are spectrometers which can be used to measure FMR at a broad range of microwave frequencies.

2.3.2.1 Vector Network Analyzer

A vector network analyzer (VNA) is a two- or four-port device which outputs and receives rf signals. It can process the magnitude and phase of the transmitted and reflected rf waves. The VNA works on the principle of sampling, in which the input signal is converted to a 100 kHz intermediate frequency signal (see Fig. 2.7 (b)), which can then be converted to digital form (Fig. 2.7 (c)). The VNA's internal computer calculates the scattering parameters, also referred to as S-parameters, or other desired quantities such as the standing wave ratio, return loss, or impedance, for example. The VNA also has the capability for error correction, with the ability to account for errors in coupler mismatch, loss, and variations in the frequency response [44].

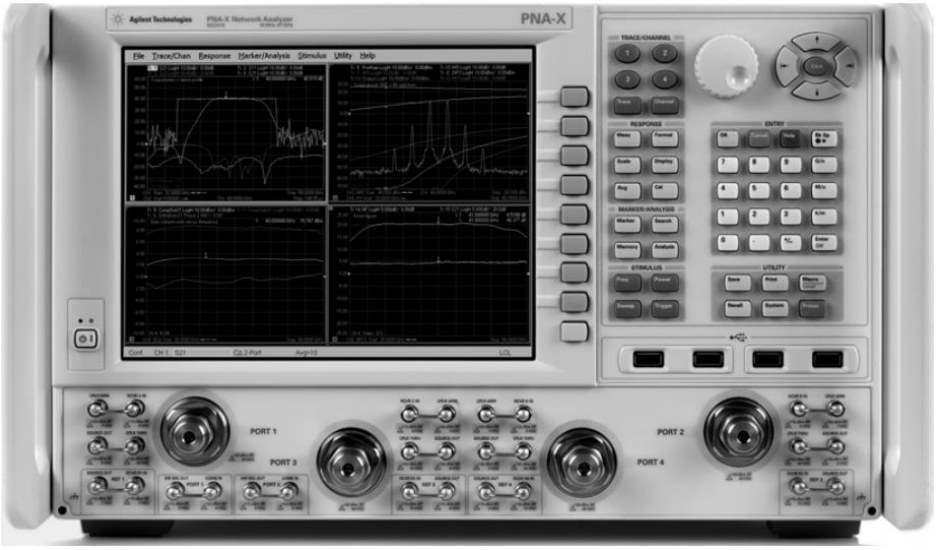

Fig. 2.6 Photograph of Agilent's N5247A Programmable Network Analyzer, used to measure the S-parameters of rf and microwave networks from 10 MHz to 67 GHz [44].

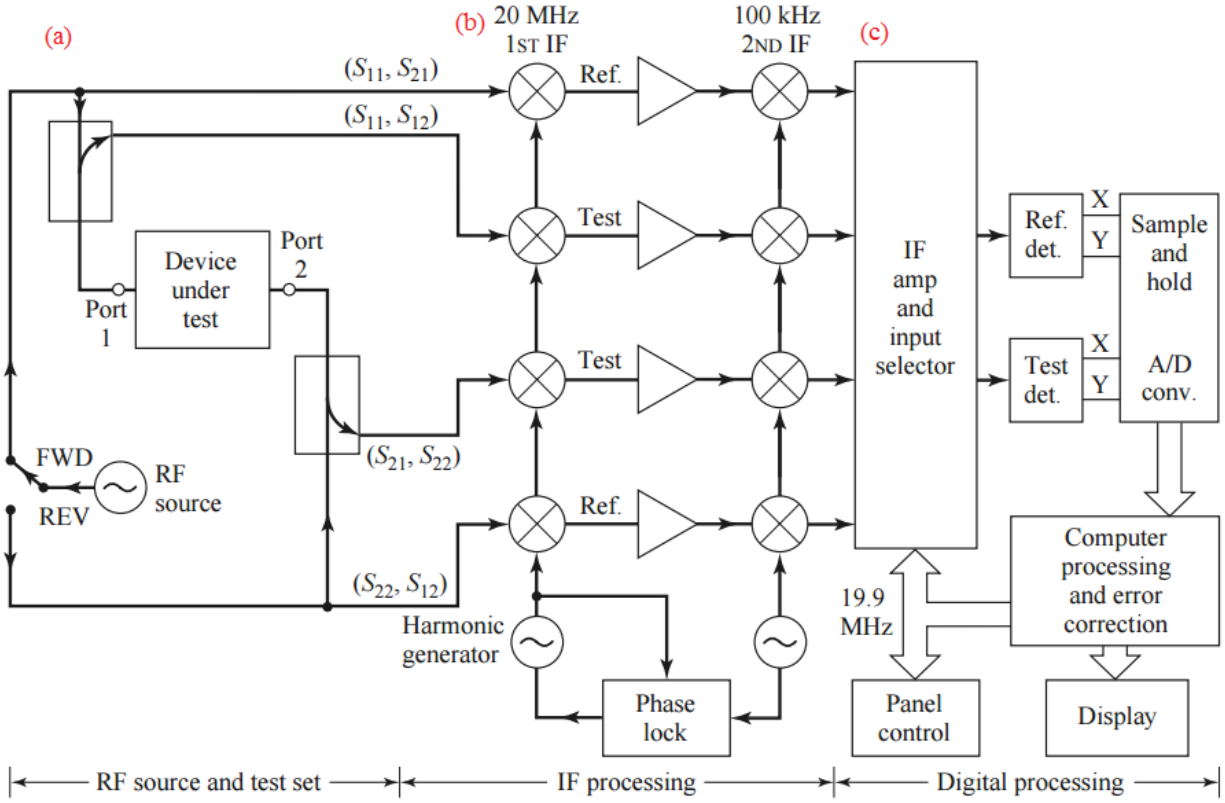

Fig. 2.7 Simplified block diagram of a VNA. (a) The rf source, output, and receiver for device testing (b) signal processing (c) digital display [44].

Our VNA is an Agilent Technologies model 8722ES, a two-port S-parameter network analyzer which operates in the range of 50 MHz to 40 GHz. The two-port design simplifies the discussion of measureable parameters.

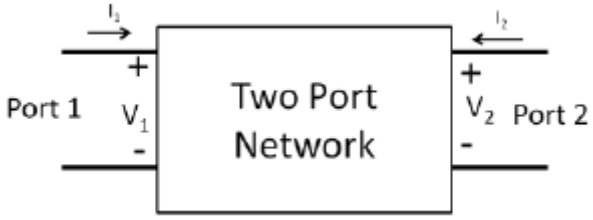

Fig. 2.8 A general two-port network

In the figure above, the two-port network is excited by voltages V_1 and V_2, and the network currents are related by the admittance matrix.

$$\begin{bmatrix} I_1 \\ I_2 \end{bmatrix} = \begin{bmatrix} Y_{11} & Y_{12} \\ Y_{21} & Y_{22} \end{bmatrix} \begin{bmatrix} V_1 \\ V_2 \end{bmatrix} \qquad 2.4$$

where the admittance matrix, [**Y**], has an inverse matrix, the impedance matrix, such that $[\mathbf{Y}] = [\mathbf{Z}]^{-1}$. If the voltages are the independent variables and the currents are the dependent, then with no additional information, four measurements are required to identify the four y-parameters. Y_{ij} is determined by applying voltage V_j at port j and short-circuiting port i, at which the short-circuit current can be measured. Similarly, one could drive port j with current I_j and open-circuit port i to measure the open-circuit voltage and find Z_{ij}. In general, Z_{ij} and Y_{ij} are complex quantities. This procedure can by extended to an N×N matrix for higher port networks.

A more convenient and simple representation of these values has been developed to analyze reflected and transmitted waves. These parameters are collected in the form of the scattering matrix. The entries in this matrix are the previously-mentioned S-parameters. This is now the more common matrix in microwave network analysis because they are easier to deal with at higher frequencies than the equivalent voltages and currents with their associated

admittance and impedance matrices. S-parameters are usually measured with the device imbedded between a 50Ω load and source. The scattering matrix is given by

$$\begin{bmatrix} V_1^- \\ V_2^- \\ \vdots \\ V_N^- \end{bmatrix} = \begin{bmatrix} S_{11} & S_{12} & \dots & S_{1N} \\ S_{21} & & & \vdots \\ \vdots & & & \\ S_{N1} & \dots & & S_{NN} \end{bmatrix} \begin{bmatrix} V_1^+ \\ V_2^+ \\ \vdots \\ V_N^+ \end{bmatrix} \tag{2.5}$$

Again, for our VNA, this is reduced to a 2×2 matrix. From the relationship

$$S_{ij} = \frac{V_i^-}{V_j^+}\,{}_{V_k^+=0 \text{ for } k\neq j} \tag{2.6}$$

the true meaning of each scattering parameter is evident.

$S_{11} = \frac{V_1^-}{V_1^+}\,{}_{V_2^+=0}$ is the input reflection coefficient with the output terminated by a matched load, $Z_L = Z_0$, so $V_2 = 0$. This is read as "voltage at port 1 from port 1". $S_{12} = \frac{V_1^-}{V_2^+}\,{}_{V_1^+=0}$ is the insertion gain with the input port terminated by a matched load. $S_{21} = \frac{V_2^-}{V_1^+}\,{}_{V_2^+=0}$ is the input transmission coefficient, the voltage output at port 2 due to input at port 1, with the output port terminated by a matched load. $S_{22} = \frac{V_2^-}{V_2^+}\,{}_{V_1^+=0}$ is the output reflection coefficient when the input port is terminated with a matched load.

The S_{21} parameter is the one of interest when studying ferromagnetic resonance, since this parameter measures transmission. The voltage at port 2 due to port 1 will drop when the resonance condition is met, indicating that some power has not been transmitted from one port to the other, but has instead been absorbed into the sample in a resonant energy transfer and will be dissipated as heat.

The data is plotted in a 3D graph with the dc field **H** on the x-axis and the microwave frequency on the y-axis. The S_{21} parameter is plotted on the z-axis. The lowest S-parameters

indicate that resonance occurred and appears as a dark curve on the graph. See Fig 2.9 (below) for an example of the FMR curve for a typical ferromagnetic material.

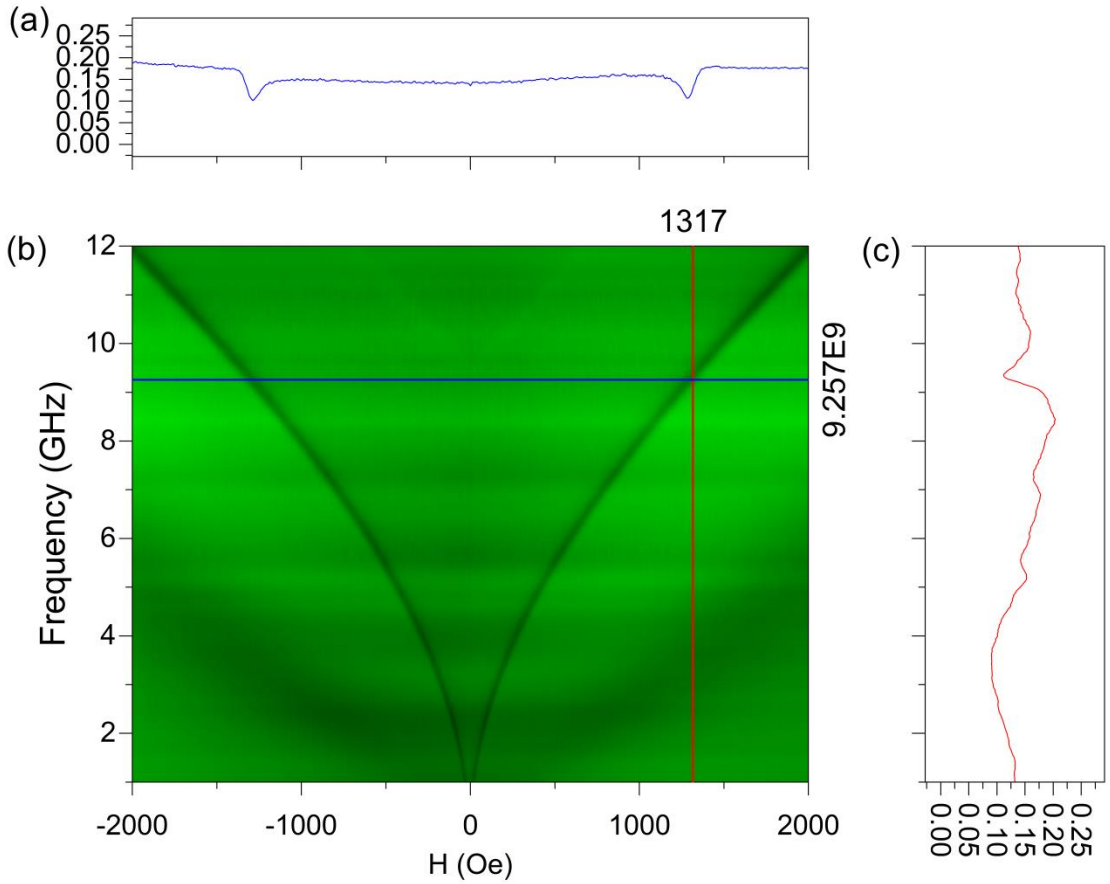

Fig. 2.9 FMR absorption in $Ni_{80}Fe_{20}$ thin film. (a) shows the S_{21} parameter as a function of applied field at the selected frequency (blue line – 9.257 GHz), (c) shows S_{21} as a function of frequency at the selected magnetic field (red line- 1317 Oe), and (b) shows the 3D graph which is a combination of the 2D graphs at every field and frequency.

Although network analyzer-FMR is the best method for broadband measurements, the VNA can also be used at individual frequencies to analyze absorption. This method will be seen in the next chapter.

2.3.2.2 Phase FMR and PPMS CryoFMR

More recently, products have been developed to perform FMR experiments at a range of temperatures, including cryogenic temperatures. PhaseFMR, by NanOsc Instruments, is a product line of several spectrometers used for this purpose. These instruments use a CPW with

direct sample contact, as in VNA-FMR rather than the resonant cavity method of the Bruker. PhaseFMR works at one frequency at a time while the magnetic field H_{dc} is swept using an external source. Unlike the Bruker, however, this spectrometer operates over a broad range of frequencies, from 2 to 16.8 GHz. The S_{21} coefficient is measured to observe resonance. A lock-in amplifier which uses phase-sensitive detection in order to capture a single component of a signal is used to filter out noise. For lock-in FMR detection, a pair of Helmholtz coils is connected to an AC source, creating a small modulation field, h_{ac}, parallel to H_{dc}.

This spectrometer has been adapted for use with Quantum Design's Physical Properties Measurement System (PPMS), in a model called CryoFMR. In this model, the size of the CPW is significantly reduced to fit within the boundaries of a PPMS insert, which contains coaxial lines which couple to the waveguide at the bottom of the insert and to the spectrometer at the top of the insert. A very small set of Helmholtz coils can be found at the bottom of the insert on either side of the CPW. The software for the instrument interfaces with PPMS MultiVu to control the magnetic field within the PPMS. Using this equipment, FMR measurements can be performed at a range of temperatures from 350 K down to 2 K.

Chapter 3: Experimental Results

This chapter introduces the type of structure studied in this work, a stack of thin film layers coupled through indirect exchange. We also report the in-plane switching behavior of our samples, followed by high-frequency characterization of our coupled magnetic systems. A custom built FMR station is described in detail, and we report a new way of representing FMR data for SAF. The resonant absorption is represented graphically in such a way as to provide a dynamic analog to the static critical curve, which is no longer valid in the presence of a microwave field. This representation is reminiscent of the initial concept of static critical curve introduced by Slonczewski [45]for a single-layer magnetic thin film. This dynamic critical curve preserves the anisotropy and characterizes the material from all directions by showing the directional dependence of absorption

3.1 Introduction to Synthetic Antiferromagnet Structures

The increasing reliance of technology on magnetic devices has led to the development of more advanced structures and systems. Synthetic antiferromagnets (SAF) are of particular interest.

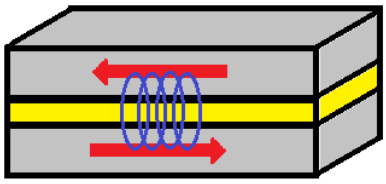

Fig. 3.1 Schematic representation of the SAF showing the two ferromagnetic layers antiferromagnetically coupled through an interlayer of non-magnetic material.

These are trilayer structures consisting of two ferromagnetic layers separated by a non-magnetic spacer and coupled through RKKY interactions. Due to shape anisotropy, thermal stability [46-49], controllable coupling strength and capacity for spin transfer [50], SAF has applications in magnetic sensors [4], perpendicular recording media [2], exchange coupled

composite media [51], and MRAM cells [49, 52, 53]. These structures consist of two ferromagnetic layers separated by a non-magnetic spacer, and are typically exchange-biased and found in stacked thin films used as magnetic tunneling junctions. The use of SAF in such applications is dependent on its interlayer exchange coupling, which determines the individual magnetic reversal of the ferromagnetic layers [54].

As seen in Chapter 1, the sign of the exchange integral determines the type of coupling (ferromagnetic or antiferromagnetic) displayed by the structure. This value is a function of separation distance between the two ferromagnetic layers. The separation is determined by the thickness of the non-magnetic spacer. Fig. 3.2 symbolically shows this concept using red and blue arrows (each corresponding to the magnetization of a layer) to indicate ferromagnetic or antiferromagnetic coupling on the curve of $J(r)$. When this type of structure is subjected to a magnetic field **H**, the magnetization vectors $\mathbf{M}_i$ of each layer do not move in unison when **H** is below the saturation field.

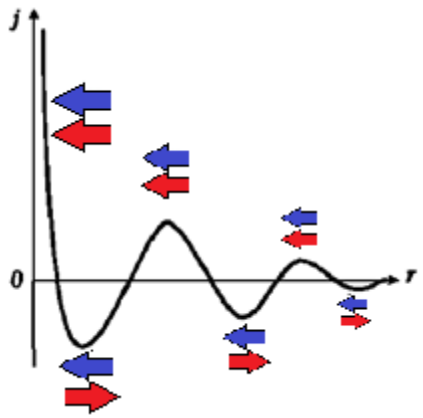

Fig. 3.2 J as a function of spacing r with arrows indicating ferromagnetic (J >0) and antiferromagnetic coupling (J < 0).

Layer switching in SAF has been extensively characterized in the past through reverse susceptibility measurements [54, 55] and simulations [56]. The dynamic properties have also been studied, either with an applied dc magnetic field directed along the easy axis [57, 58], or in

such a way as to identify resonant absorption per layer in multilayered devices which include a SAF [59].

3.1.1 Hysteresis in SAF

SAF structures have very distinctive hysteresis loops. In fact, the MHL is the quickest and easiest way to identify the type of coupling and strength when the RKKY exchange is present in a stacked sample. While the MHL for a typical ferromagnetic sample follows the single-step path seen in Fig. 2.1, a SAF will typically show multi-step behavior.

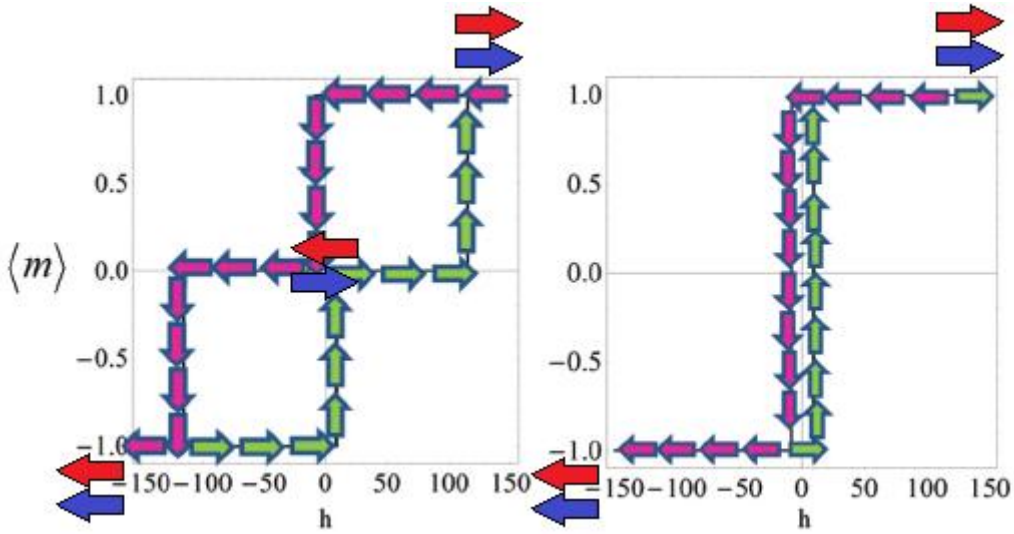

Fig. 3.3 Simulation with path direction for structures displaying antiferromagnetic coupling (left) and ferromagnetic coupling (right) [60]. The red and blue arrows represent the magnetization of each layer at different points on the MHL.

3.1.2 SAF Applications

The indirect coupling of ferromagnetic materials across a non-magnetic layer has been investigated for its various applications since 1986 [61]. In this section, we will briefly discuss some applications of SAF.

SAF has very successfully been used as the soft under-layer of recording media due to enhanced thermal stability [62, 63]. The bottom layer couples antiferromagnetically to the top (recording) layer through a thin spacer. This has advantages over single-layer media because the

effective M_rt (where M_r is remanence magnetization and t is thickness) is reduced. Thermal stability is enhanced due to the exchange coupling. One study has reported that the strength of exchange coupling may be further increased by increasing the thickness of the bottom layer [64].

In magnetic tunnel junctions (MTJ), a (pinned) hard magnetic layer is separated from a (free) soft magnet by a non-magnetic insulator. MTJs are suitable for high density read head and magnetic random access memory (MRAM) applications, where the MTJ may be found in sub-micron cells. As the size of the cells decrease, a larger switching field, H_{Sw}, is required because the demagnetizing field from the cell edges will be larger. SAF structures have been used to reduce the required H_{Sw}.

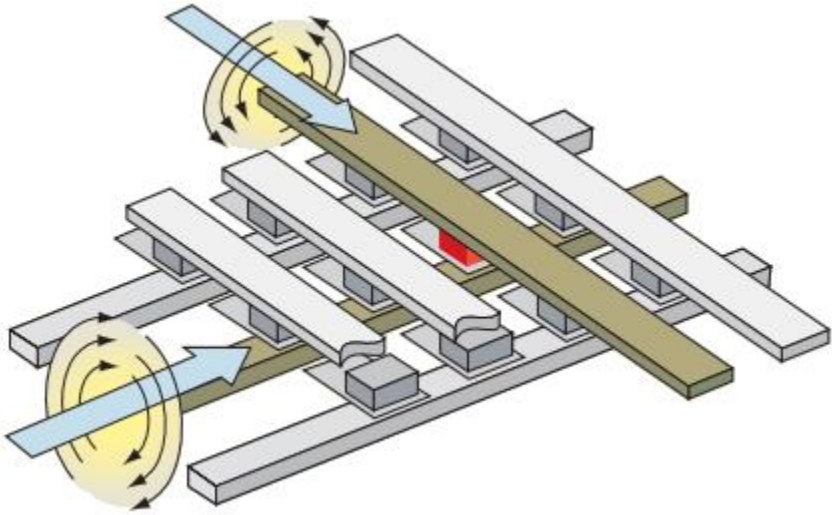

Fig. 3.4 MRAM write operation [65]

One of the most important applications of SAF is to MRAM and toggle-MRAM [20]. Fig. 3.4 shows the write operation of MRAM. The selected MTJ (highlighted in red) is positioned between the selected word line (WL) and bit line (BL), shown in green. Current is applied in the direction of the blue arrows, creating a magnetic field around the line. The vector sum of these fields at the position of the MTJ must be large enough to switch its state, while the lone fields of the WL and BL must be small enough to never switch the state of the half-selected

MTJs that lie along the selected WL and BL. The astroid describes the switching behavior of the free layer.

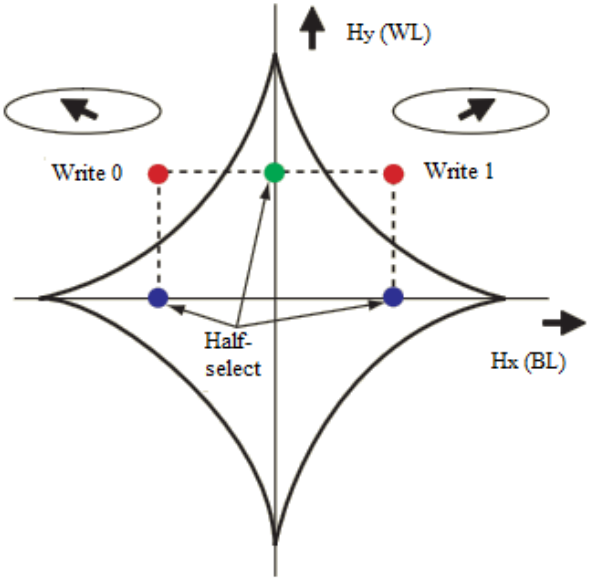

Fig. 3.5 Ideal critical curve describing the switching in the MTJ free layer

Fig. 3.5 shows the ideal switching curve of the MJT free layer. If the applied field begins at the origin, increases to a point to the right of the y-axis and outside the astroid, and then returns to the origin, the free layer will be magnetized to the right, or data state 1. If it begins at the origin and moves left of the astroid, the free layer will be magnetized to the left, data state 0. If the field remains inside of the astroid, the MTJ's state is unchanged. In summary, to successfully write, the fully selected fields must lie outside of the astroid, and the half-selected fields must remain within the astroid.

It is important to emphasize that the astroid depicted in the figure is an *ideal* switching curve. The real curve will vary dependent on the individual MTJ. The ability to reliably write without disturbing the other components is degraded by this variation. Further, there is a chance that operations close to the curve boundary may undergo thermally activated switching [66]. In response to these problems, the "toggle-mode" MTJ has been developed [53]. This structure is

similar to the traditional MTJ except that the free layer consists of two (weakly) antiferromagnetically coupled layers.

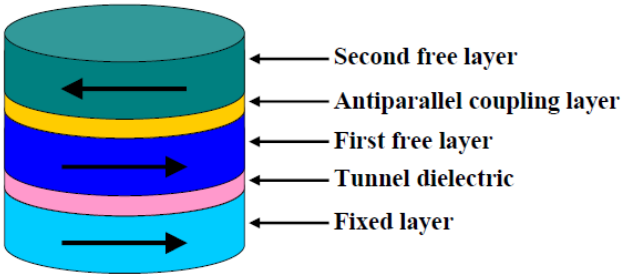

Fig. 3.6 Toggle MTJ structure [20].

The toggle-mode MTJ differs from the traditional in that it does not write directly into one state or another; rather, it toggles its state when exposed to similar WL and BL current pulse sequences. The dipoles of the free layer magnetization rotate in the direction of the applied field and follow the applied field as it rotates during the current pulses. At the end of the sequence, the diploes have rotated 180º from its initial orientation. The device will toggle successfully as long as the applied field traces a path in its plane that contains the so-called "spin-flop" point. This type of device is impervious to half-select disturbs, since these disturbs do not trace the path enclosing the spin-flop point. Additionally, since the free layer has no net magnetic moment, each device is undisturbed by the state of adjacent devices.

3.1.3 Sample Description

The samples studied were trilayered thin films deposited onto a glass substrate. These samples were provided by Dr. Ganping Ju of Seagate Technology, Pittsburg, PA. The bottom ferromagnetic layer is FeCoB, the second is the non-magnetic spacer composed of Ru, and the top ferromagnetic layer is again FeCoB, followed by a C overcoat for surface protection. The samples were deposited at room temperature with DC magnetron sputtering with a base vacuum pressure below 3×10^{-9} Pa. The sample size is 5×5 mm^2. The thickness of the Ru spacer was

varied among a series of samples in the range of 8 to 20 Å. The exact value of Ru thickness (t_{Ru}) required to provide antiferromagnetic coupling between the ferromagnetic layers was not precisely known beforehand. Therefore, only a few of the samples produced were actually SAF structures.

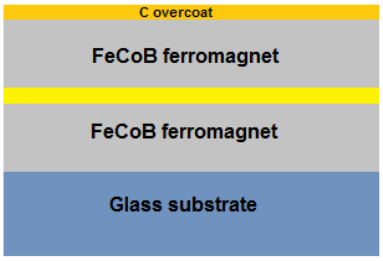

Fig. 3.7 SAF sample structure (not to scale)

Of the seven samples, four were selected for the high frequency characterization study so as to cover all types of RKKY coupling. The first sample chosen has t_{Ru} = 8 Å. It is one of four samples which are coupled ferromagnetically. The next two samples have t_{Ru} = 14 Å and t_{Ru} = 16 Å. Both of these samples are coupled antiferromagnetically. The final sample of the series, t_{Ru} = 18 Å, shows antiferromagnetic coupling with asymmetric layer switching. The naming convention of these samples is "R(t_{Ru})". Fig. 3.8 shows the hysteresis in all seven samples and illustrates the evolution of the indirect exchange as a function of t_{Ru}. The MHLs were measure using Lake Shore's PMC MicroMag 3900 VSM.

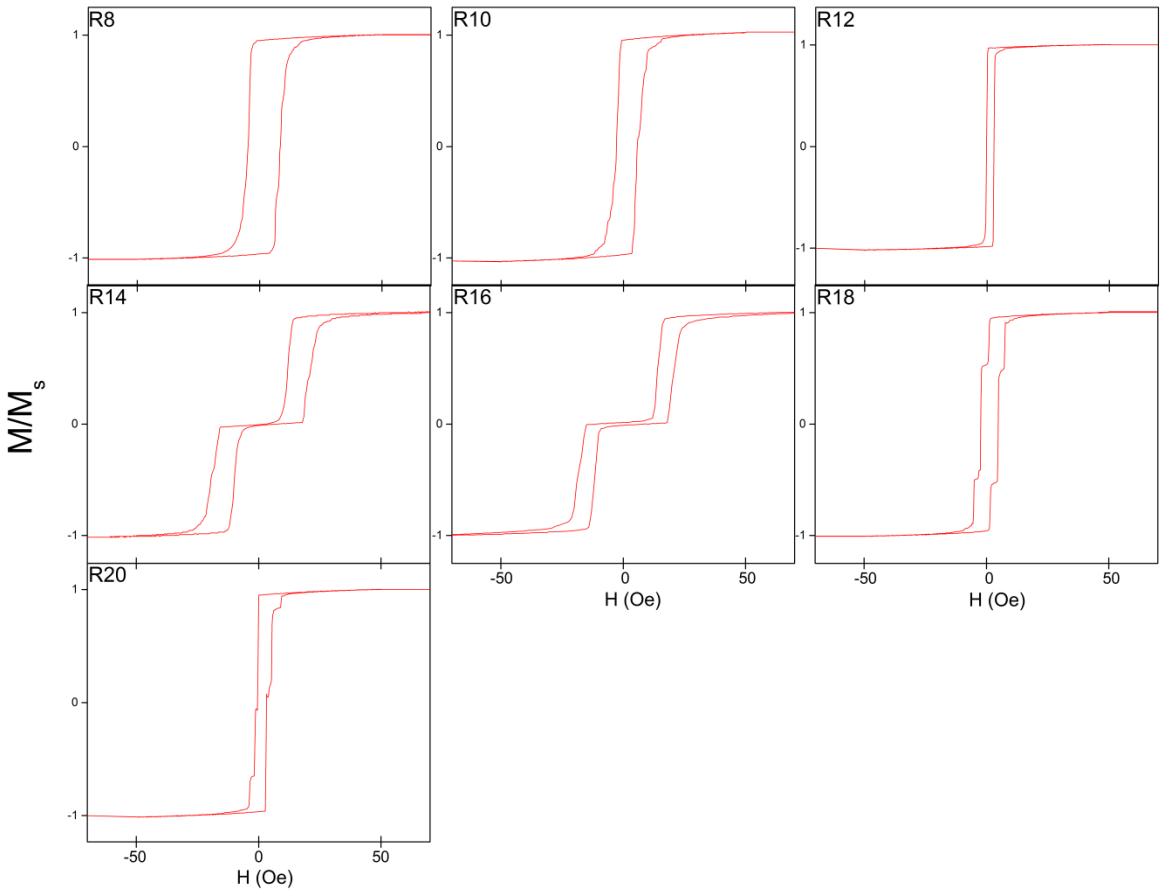

Fig. 3.8 MHL of all SAF samples in the series. The applied field is along the easy axis in all MHLs. *J* is observed to move from positive to negative and back towards positive again as t_{Ru} increases

3.1.4 Free Energy and Magnetization Dynamics in SAF

The free energy in a SAF structure, in general, includes a contribution from the Zeeman energy term, the uniaxial anisotropy in the plane of the sample, shape anisotropy, out-of-plane anisotropy, and the exchange term. For our samples, magnetization was always in the plane of the sample.

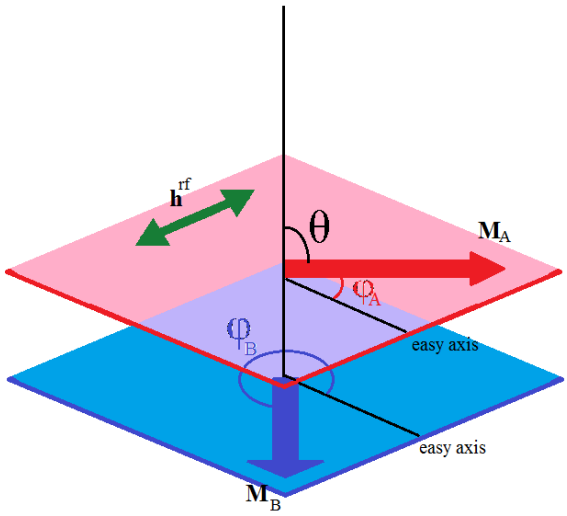

Fig. 3.9 Schematic diagram of the ferromagnetic layers of the SAF structure. The magnetization vectors are in the plane of the sample and defined by the angles θ (from the sample's normal line to the vector) and φ_A and φ_B (from the easy axis to the vector in the top and bottom layer, respectively).The applied field (not shown) is in the plane of the sample, as is the rf magnetic field for the FMR measurements.

The anisotropies have an in-plane easy axis along $\varphi = 0°$. An external field **H** is applied at some angle φ_H with respect to the easy axis. The normalized energy density of the φ-dependent terms is

$$E(\varphi) = -MH\cos(\varphi_H - \varphi_i) - 2K\cos^2\varphi_i \tag{3.1}$$

where the subscript i refers to the top and bottom layers, A and B respectively, and the anisotropy constant $K = MH$. The energy of each layer can be normalized to get

$$\eta_A = -H\cos(\varphi_H - \varphi_A) - \frac{1}{2}H_K^A\cos^2\varphi_A \tag{3.2}$$

$$\eta_B = -H\cos(\varphi_H - \varphi_B) - \frac{1}{2}H_K^B\cos^2\varphi_B \tag{3.3}$$

A visual representation of φ_A and φ_B are given in Fig. 3.9. The energy due to the interaction is given by

$$E_{\text{int}} = -J_1\frac{\mathbf{M_A}\cdot\mathbf{M_B}}{|\mathbf{M_A}||\mathbf{M_B}|} - J_2\left\{\frac{\mathbf{M_A}\cdot\mathbf{M_B}}{|\mathbf{M_A}||\mathbf{M_B}|}\right\}^2 \tag{3.4}$$

or, equivalently,

$$E_{\text{int}} = -J_1 \cos(\varphi_{\text{A}} - \varphi_{\text{B}}) - J_2 \cos^2(\varphi_{\text{A}} - \varphi_{\text{B}}) \quad 3.5$$

where J_1 and J_2 are the bilinear and biquadratic coupling constants between the two layers, respectively [67]. Normalizing eq. 3.5,

$$\eta_{\text{int}} = -H_1^J \cos(\varphi_{\text{A}} - \varphi_{\text{B}}) - H_2^J \cos^2(\varphi_{\text{A}} - \varphi_{\text{B}}) \quad 3.6$$

where $H_1^J = \frac{J_1}{tM_s}$ and $H_2^J = \frac{J_2}{tM_s}$ with t being the thickness of the layers.

The LLG equation for the system is

$$\frac{d\mathbf{M_i}}{dt} = -\gamma(\mathbf{M}_i \times \mathbf{H}_i) + \frac{\alpha_i}{M_s}\left(\mathbf{M}_i \times \frac{d\mathbf{M}_i}{dt}\right) \quad 3.7$$

which can be expressed in angular coordinates [58]

$$\frac{d\theta_i}{dt} = \frac{\gamma}{1+\alpha_i^2}(H_{\varphi i} + \alpha_i H_{\theta i}) \quad 3.8$$

$$\sin\theta_i \frac{d\varphi_i}{dt} = \frac{\gamma}{1+\alpha_i^2}(\alpha_i H_{\varphi i} - H_{\theta i}) \quad 3.9$$

with H_θ and H_φ as the components of the effective field. These components are expressed as

$$H_{\theta i} = -\frac{1}{M_s}\frac{\partial E}{\partial \theta_i} + \mathbf{h}^{\text{rf}} \cdot \hat{\theta}_i \quad 3.10$$

$$H_{\varphi i} = -\frac{1}{M_s \sin\theta_i}\frac{\partial E}{\partial \varphi_i} + \mathbf{h}^{\text{rf}} \cdot \hat{\varphi}_i \quad 3.11$$

where $\mathbf{h}^{\text{rf}}$ is the dynamic component of the external field, and $\hat{\theta}_i$ and $\hat{\varphi}_i$ are the unit vectors [58]

$$\hat{\theta}_i = \cos\varphi_i \cos\theta_i \hat{x} + \sin\varphi_i \cos\theta_i \hat{y} - \sin\theta_i \hat{z} \quad 3.12$$

$$\hat{\varphi}_i = -\sin\varphi_i \hat{x} + \cos\varphi_i \hat{y} \quad 3.13$$

Since the magnetization vectors in our samples are in the plane of the layers, the angles $\theta_i = \frac{\pi}{2}$, so $\sin\theta_i = 1$, which means eqs. 3.12 and 3.13 are now quite similar in form to one another. A convenient representation of this form of data was introduced by Gonzalez-Chavez [58]:

$$\begin{bmatrix} \dot{\theta}_A \\ \dot{\varphi}_A \\ \dot{\theta}_B \\ \dot{\varphi}_B \end{bmatrix} = -\frac{\gamma}{M_s}[\mathbf{\Lambda}] \begin{bmatrix} \partial E/\partial\theta_A \\ \partial E/\partial\varphi_A \\ \partial E/\partial\theta_B \\ \partial E/\partial\varphi_B \end{bmatrix} + \gamma[\mathbf{\Lambda}] \begin{bmatrix} \mathbf{h}^{\mathrm{rf}} \cdot \hat{\theta}_A \\ \mathbf{h}^{\mathrm{rf}} \cdot \hat{\varphi}_A \\ \mathbf{h}^{\mathrm{rf}} \cdot \hat{\theta}_B \\ \mathbf{h}^{\mathrm{rf}} \cdot \hat{\varphi}_B \end{bmatrix} \quad 3.14$$

where the matrix $[\mathbf{\Lambda}]$ has been introduced as

$$[\mathbf{\Lambda}] = \begin{bmatrix} \frac{1}{1+\alpha_A^2}\begin{pmatrix} \alpha_A & 1 \\ -1 & \alpha_A \end{pmatrix} & 0 \\ 0 & \frac{1}{1+\alpha_B^2}\begin{pmatrix} \alpha_B & 1 \\ -1 & \alpha_B \end{pmatrix} \end{bmatrix} \quad 3.15$$

3.2 Static Critical Curve of SAF

The static critical curves for the SAF samples had been obtained by the TDO method. In this way, the points of magnetization switching in the SAF samples were obtained. These points were plotted on a polar chart to create the critical curve for the samples. For SAF, the critical curve contains two envelopes. The outermost envelope describes the saturation field, in which both layers have a magnetization parallel to one another, while the inner contains the critical fields for switching.

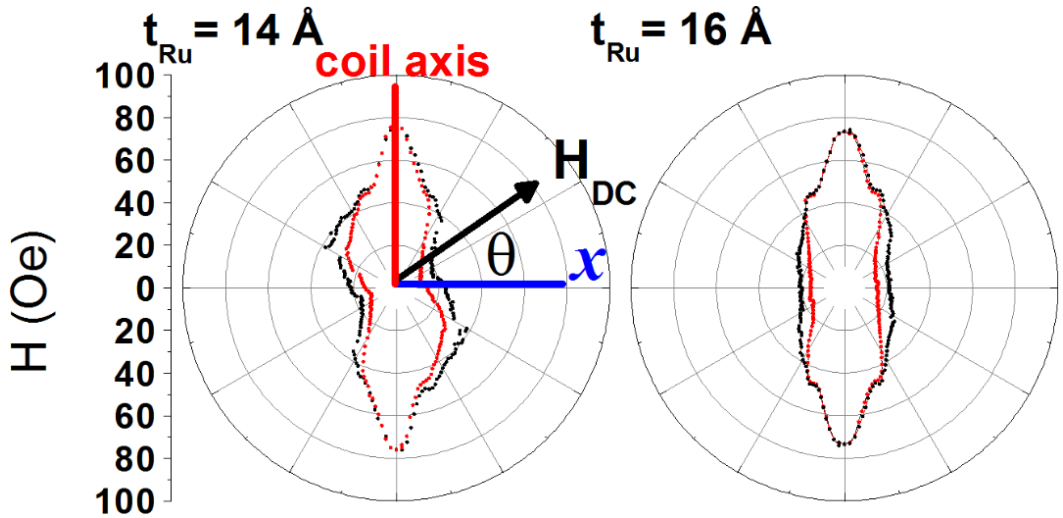

Fig. 3.10 Critical switching curves for SAF samples obtained through TDO method.

The dc magnetic field was created using a stationary double Helmholtz coil and controlling the current in each coil to create a uniform field in the desired direction. The reverse susceptibility signal was recorded for different orientations of the dc field from 0º to 180º with respect to the sensing coil axis in 2º increments. The dc field was swept first from positive saturation to negative, and then from negative saturation to positive, so as to obtain a complete 360º characterization.

3.3 Dynamic Critical Curve of SAF

3.3.1 Custom Experimental Setup for FMR Measurements

A new experimental setup for the FMR measurements was fully designed and constructed for this project. It was built on CleanTop® Breadboard manufactured by TMC by with four TMC vibration isolators and accessories from Newport. It was adapted to have a second level which is fully equipped for mounting equipment, as is the lower level. The bottom level includes a rotation stage which is housed on a Newport lab jack with x- y- and z-translation. The rotation stage supports a GMW 5201 Projected Field Electromagnet. The setup also includes the required chiller and water flow control, as well as a Kepco Bipolar Power supply, 20V, 20A to power the magnet. A full LabVIEW program was built to control the devices and record the output data.

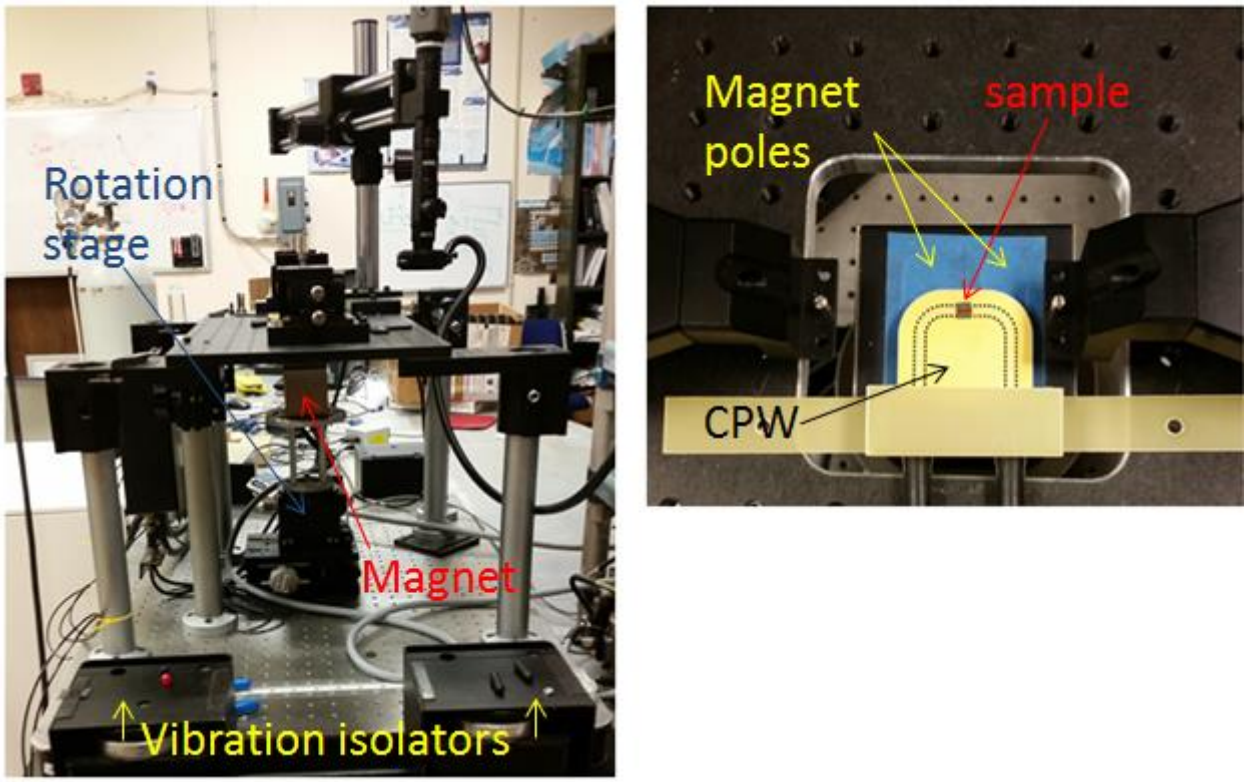

Fig. 3.11 *Left*: Probe station with vibration isolators, magnet, rotation stage, and microscope. *Right*: CPW above magnet with sample in place.

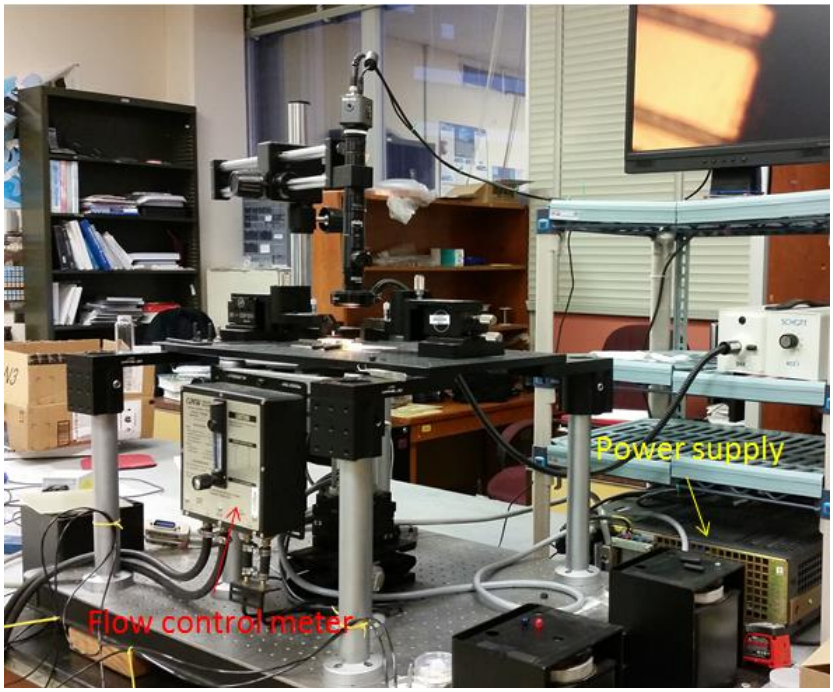

Fig. 3.12 Probe station showing power supply and water flow control.

The top level supports the sample stage and probe station. This probe station is designed such that the VNA can couple with one of two different types of coplanar waveguide (CPW). When using a micron-scale CPW fabricated through photolithography, the user will take advantage of the probe mounts using the Model 40A GGB Industries High Performance Microwave Probes with a G-S-G configuration. For landing the probe tips on the CPW, a microscope with a display monitor and light is available.

In this type of measurement, the ac microwave signal produced by the VNA and transmitted through the CPW has a magnetic component which is in a direction perpendicular to the dc field. A positive-saturating dc field is applied and microwave frequencies are scanned in the desired frequency range. The S_{21} transmission coefficient is recorded as a function of frequency. The dc field is the incremented and the frequency scan is performed again.

In the case of our SAF structures, the sample area is 5×5 mm^2, so the micron-scale CPW is not an option for these samples. For these measurements, a larger CPW is used. The CPW is mounted in a plastic holder to ensure proper repositioning after removing and reinstalling. The holder suspends the sample at a height of 0.5 to 1 cm above the magnet. This height is required so that the magnet has room to rotate beneath the sample area. The microwave properties of the four selected structures were studied first through broadband FMR measurements with the dc magnetic field applied parallel to the sample's easy axis.

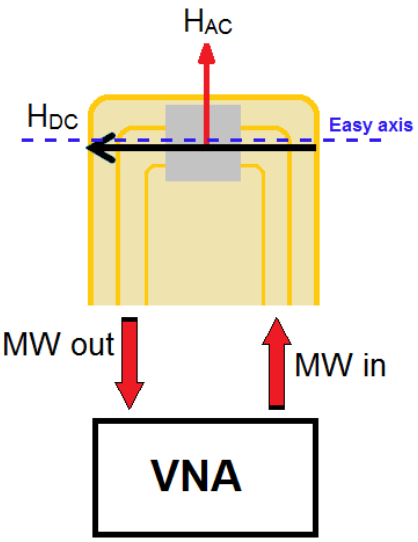

Fig. 3.13 Representation of sample on CPW (not to scale) with dc field parallel to the easy axis and perpendicular to the magnetic component of the microwave field.

3.3.2 Broadband FMR Measurements

For the four selected FeCoB trilayer samples, a positive dc saturating field of 500 Oe was applied and microwave frequencies were scanned in the range 500 MHz to 8 GHz. The S_{21} parameter was recorded as a function of frequency. The dc field was decremented by 2 Oe after each frequency sweep down to a field of -500 Oe.

In the case of a true SAF sample, the broadband FMR curve is observed to "split" at lower fields, rather than almost merging together at some minimum field as is typically seen in the absorption curves in a ferromagnetic material. This splitting can be anticipated, based on the shape of the MHL. As expected, the curve of sample R8 is almost indistinguishable from a more typical ferromagnetic thin film – just as its MHL is almost indistinguishable from a typical ferromagnetic thin film, while R14 and R16 show obvious splitting. This separation in the broadband curve matches up exactly with the separation of the MHL. For R18, the steps in the hysteresis loops are very close together (less than 5 Oe apart) so the broadband splitting is not as clear as it is for the true SAFs, however, it can be seen if one looks carefully (see Fig. 3.14).

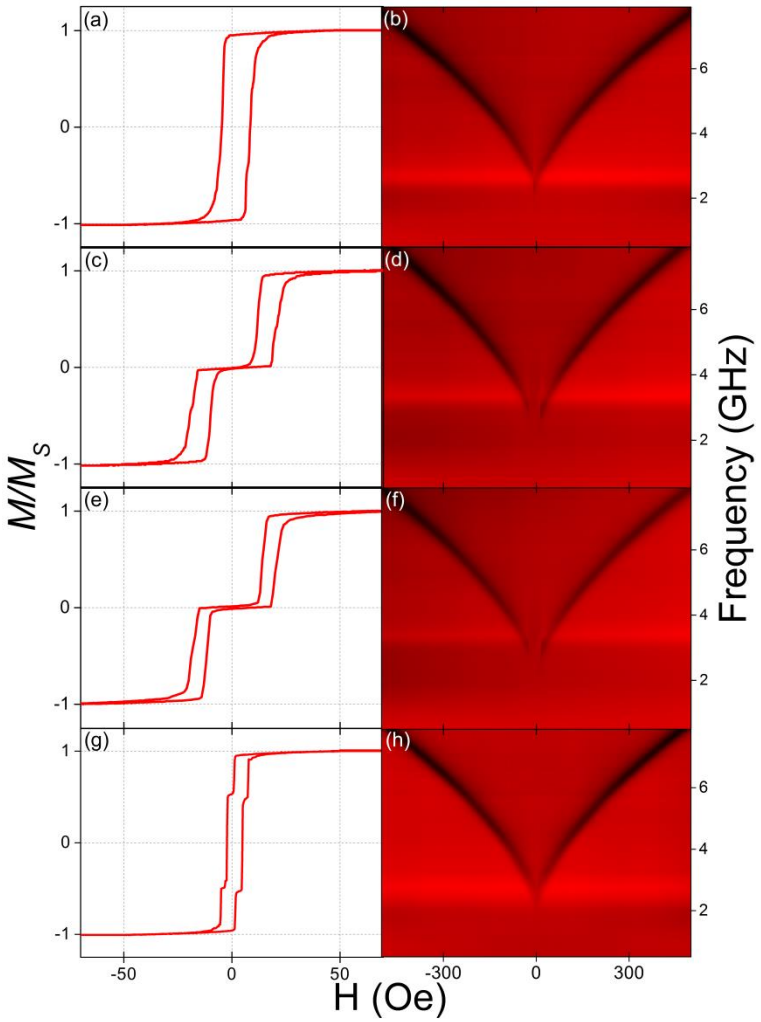

Fig. 3.14 MHLs (a,c,e,g) and broadband FMR (b,d,f,h) for samples R8 (a,b), R14 (c,d), R16 (e,f) and R18 (g,h).

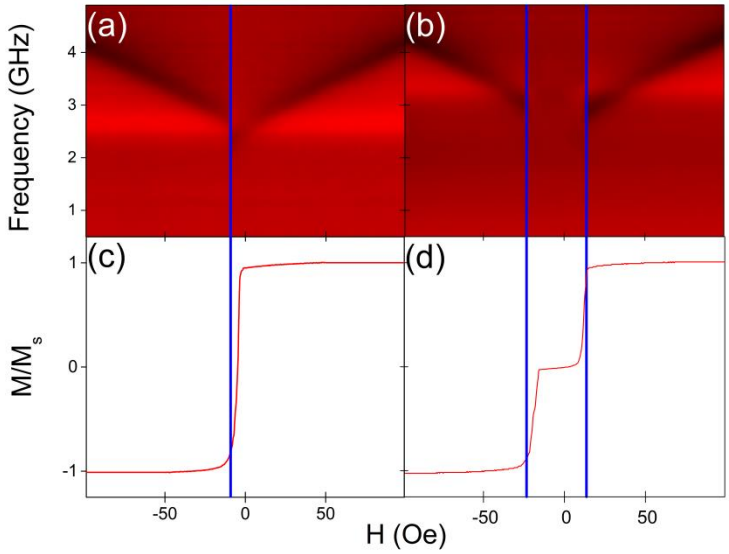

Fig. 3.15 Broadband FMR compared to the descending half of the MHL for R8 (a,c) and R14 (b,d).

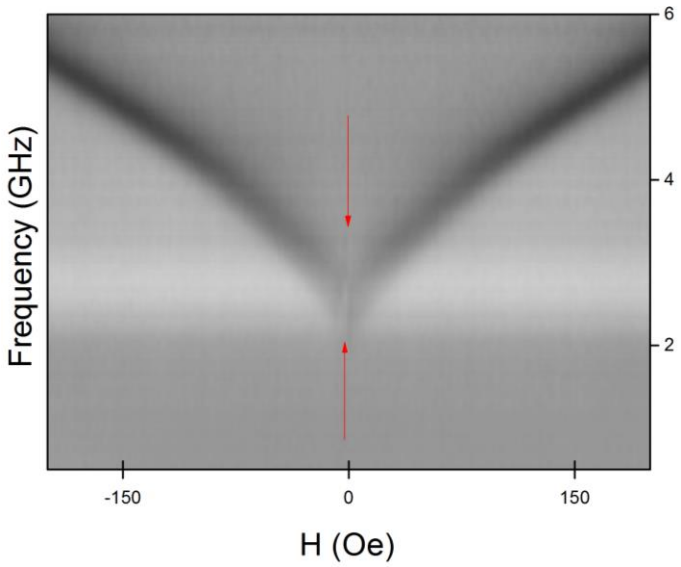

Fig. 3.16 Broadband FMR for R18

With the broadband curves completed, we were able to clearly see the more interesting ranges in the absorption spectra. The VNA was then set to measure the S_{21} parameter at a fixed frequency while the magnetic field was swept from a maximum positive value to negative along the easy axis in order to see the absorption profile for a particular frequency. This measurement was repeated for every sample at a minimum of four different frequencies (six for the true SAF samples). In this way, we could compare the evolution of FMR absorption of the SAF to the others. One can immediately see (Fig. 3.15) that the exchange interaction is evident at the lower

frequencies, while at higher frequencies the curves become more comparable. The lower frequency scans offer a clearer look at the FMR absorption in the splitting region of the broadband curve.

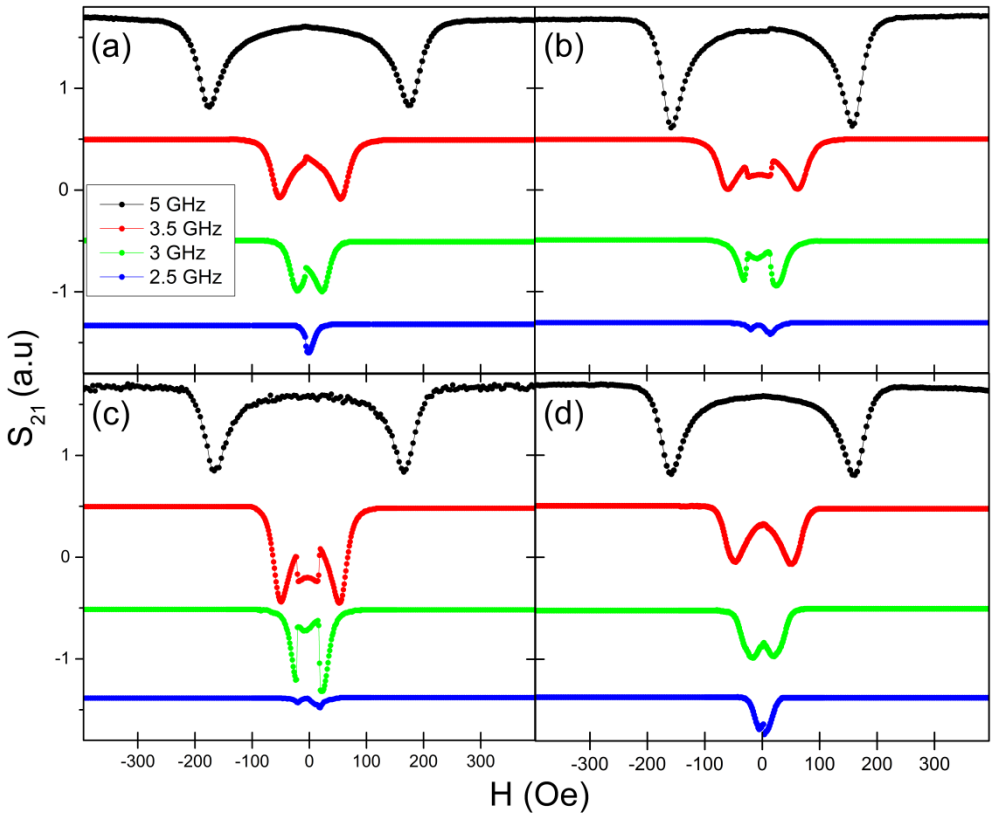

Fig. 3.17 Constant-frequency FMR measurements for different frequencies and t_{Ru}, with the dc magnetic field applied along the easy axis and perpendicular to the microwave magnetic field for (a) R8, (b) R14, (c) R16, and (d) R18. The data have been artificially shifted along the (arbitrary) vertical axis.

Although data shown in this subsection are useful to characterize the easy axis of our sample, these representations do not tell us anything about the sample's anisotropy. In the next subsection, a new method for displaying the FMR data for SAF is offered. This new method, as we will see, completely characterizes the angular dependence of FMR for our samples.

3.3.2 Constructing the Critical FMR Curve

It has been shown that the switching behavior in magnetic nanostructures can be studied through FMR measurements with an angular variation of the dc magnetic field [68]. The

purpose of these angular-dependent FMR measurements is to capture information about the anisotropy. In the case of uniaxial anisotropy, as applies to our samples, absorption will occur at some minimum dc field along the easy axis, and a maximum field along the hard.

These measurements are performed in a similar way to the continuous-wave (CW) frequency FMR measurements discussed previously, with one addition. The measurements were performed with the microwave magnetic field of the CPW directed along the samples' hard axis, while the dc magnetic field is applied in the plane of the samples at a sequence of angles θ relative to the easy axis. For each angle, the applied dc magnetic field was swept from positive saturation, through zero, to negative saturation. The measurement of the S_{21} parameter was repeated at each increment of the dc field. These measurements were repeated as a function of θ in the range of 0º to 360º in increments of 5º. The data was then plotted in a polar contour chart, with the r-axis having the values of dc field, the angular axis being the angle θ measured with respect to the easy axis, and the z-axis as the S_{21} parameter. These polar charts were constructed for all four samples for a minimum of four different frequencies per sample (again, six in the case of actual SAF).

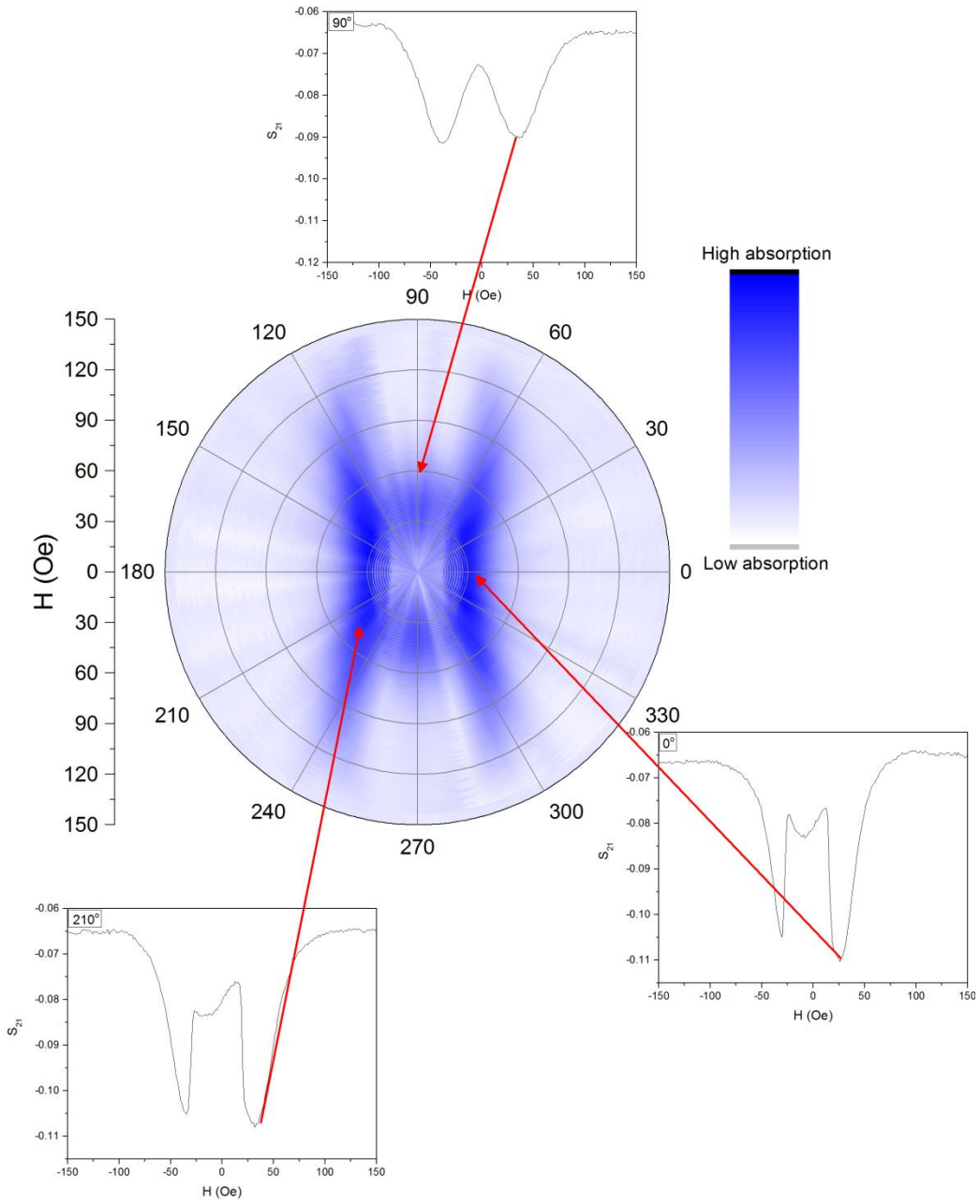

Fig. 3.18 Polar representation of FMR for sample R14 at a microwave frequency of 3.0 GHz. Examples of S_{21} as a function of H are included to give an idea of how these graphs make up the polar contour. The easy axis is along 0°, the rf magnetic field is along 90°, and the dc magnetic field is applied at θ to the easy axis.

All of the information provided by the systematic, angle-dependent CW FMR measurements is contained in a compact polar representation which completely characterizes the angular dependence of FMR. This is a much better way to see the full high-frequency

description of an anisotropic structure, rather than looking at dozens of graphs in the form of a 2D CW scan (Fig. 3.15).

As seen in the above figure, R14 (and R16 as we will see) displays an inner envelope, the result of the small absorption seen in the CW measurement, which is explained by the fact that the magnetization vectors of each layer do not move in unison but rather, at some point in the magnetization, act individually. A ferromagnetically coupled sample will not show this inner envelope.

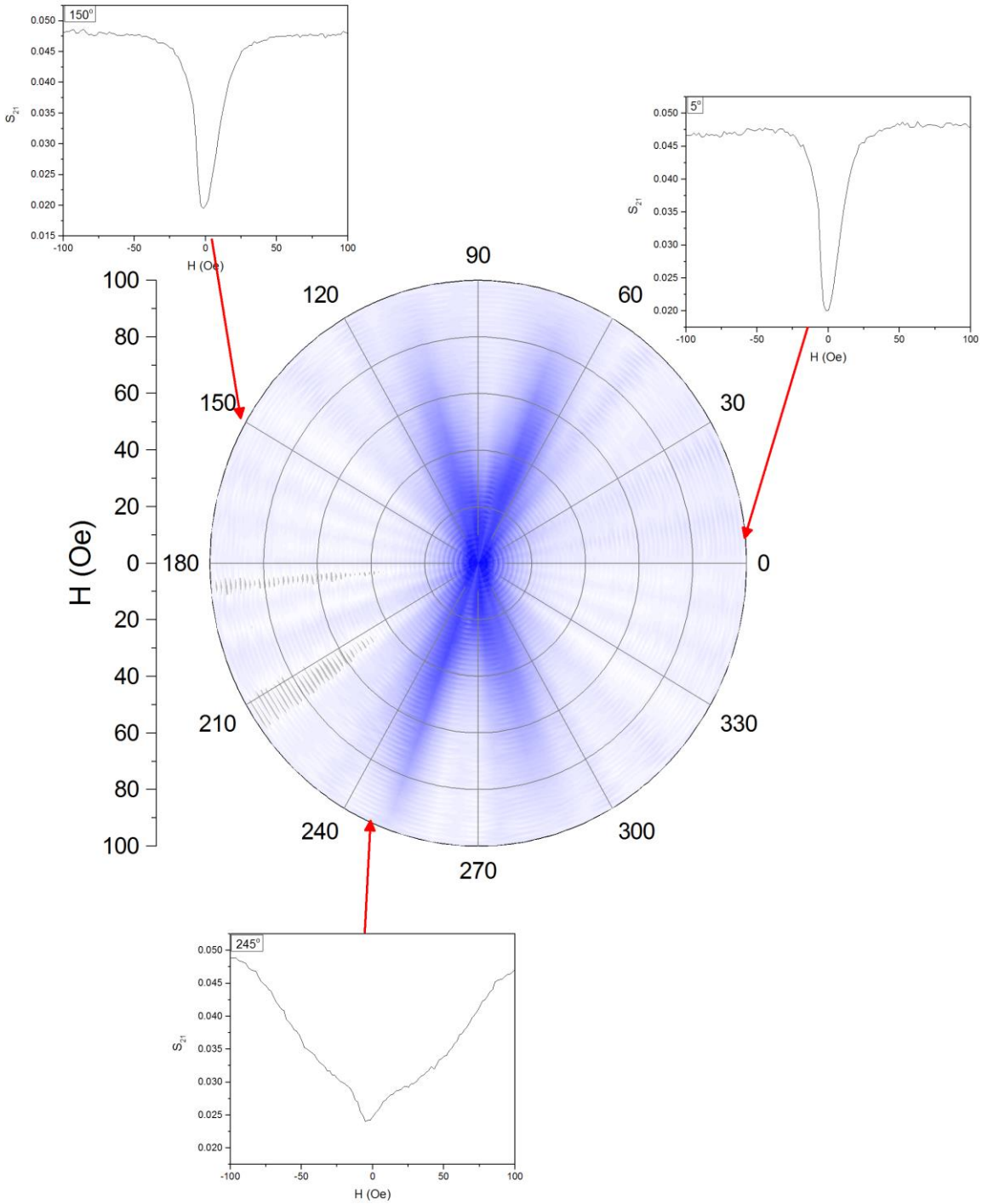

Fig. 3.19 Polar representation of FMR for sample R8 at a microwave frequency of 2.5 GHz. Examples of S_{21} as a function of **H** are show. The inner envelope is not observed as it is with sample R14. It is also important to note the presence of only one absorption peak rather than one for positive fields and one for negative fields. The reason for this is that this measurement is very close to the lowest possible FMR frequency observed, i.e., the peak of the broadband curve.

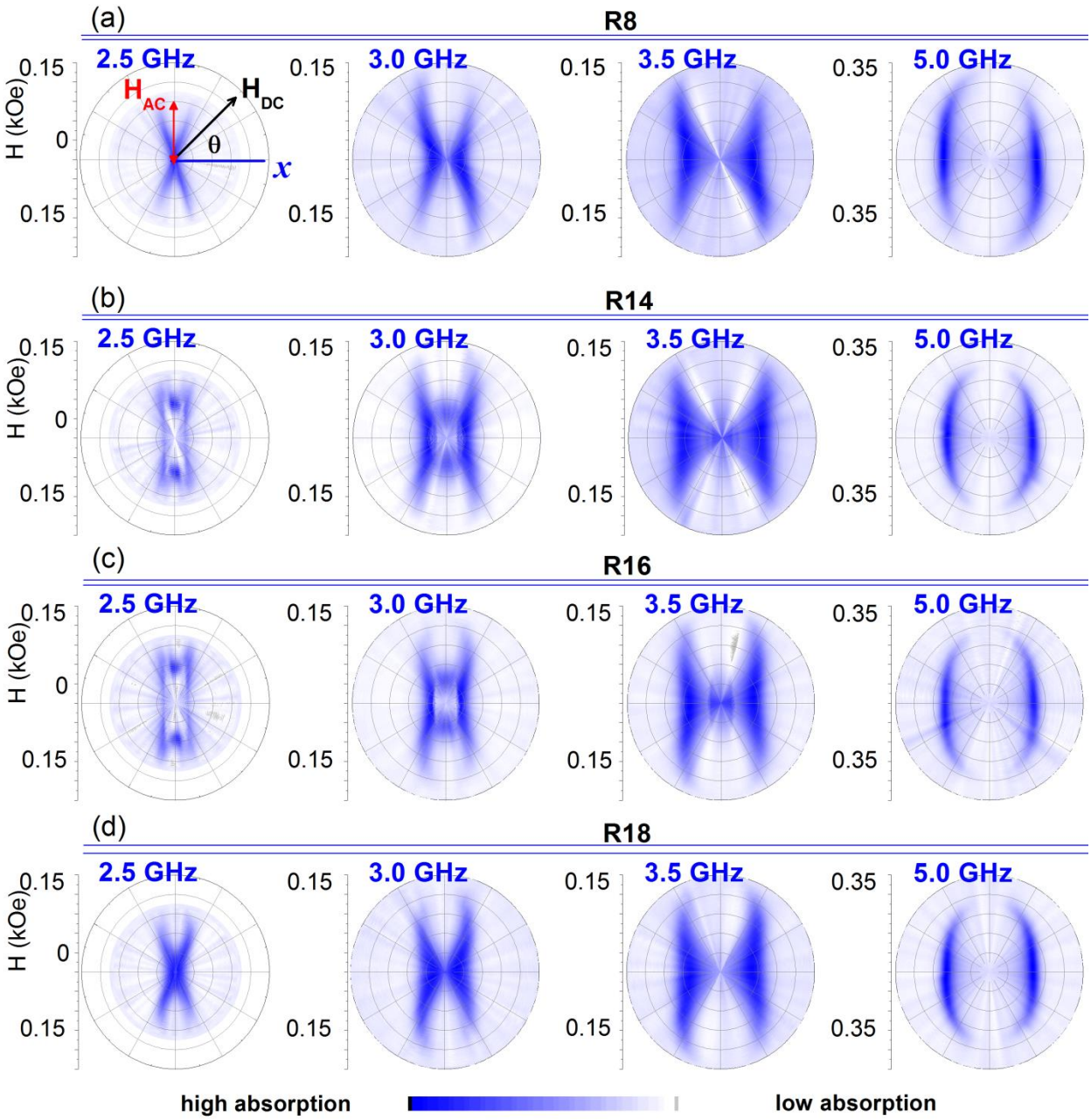

Fig. 3.20 Polar contour graphs of experimental CW FMR measurements for different frequencies and t_{Ru}, with the dc magnetic field applied at different angles θ relative to the easy axis for (a) R8, (b) R14, (c) R16, and (d) R18. For all samples, the easy axis is directed along ***x***.

As expected from the CW graphs of Fig. 3.15, the polar contours for SAF are quite different than the polar contours for ferromagnetically-coupled trilayers at lower frequencies. At higher frequencies (~3.5GHz), they become less distinguishable, and at 5 GHz, they are practically identical. This confirmed our thoughts from the beginning, that for higher

frequencies the angular curve becomes more isotropic and tends toward a more circular shape [68]. In the low-frequency graphs, one can quickly identify anisotropy effects, observing that the lowest resonant fields are along the easy axis. Interaction effects can also be identified comparing the polar resonant absorption curves between samples.

Chapter 4: Discussion and Conclusion

In this chapter, we will revisit a theory mentioned in Chapter 2, which proved theoretically that TS is the lowest limit of FMR. We will see how the polar representation of FMR will help us see the validity of this theory.

4.1 Transverse Susceptibility as the Low-Frequency Limit of FMR

Both TS and FMR are magnetization processes in perpendicular magnetic fields, though they are distinct techniques. TS refers to experiments in perpendicular fields of low frequency while FMR deals with higher frequency experiments. However, the distinction between the two is artificial, as shown in ref. [41].

The TS tensor is complex and can be written as $\chi_t = \chi_t' + i\chi_t''$. χ_t' and χ_t'' are real functions dependent on angular frequency ω. When $\omega = 0$, the real part of TS exhibits a singularity for $H_{DC} = H_K$. As the ac frequency increases, the singular peak at H_K splits into two resonant peaks for which TS changes sign and vanishes. The field values at which the real part of TS vanishes are exactly the field values for which FMR occurs for the corresponding resonant frequency.

4.2 Evolution from TS to FMR

For our samples, the H_{DC} which satisfied the resonance condition was approximately constant for frequencies from 2.5 GHz and below (see Fig. 4.1), although FMR below 2.5 GHz had such small amplitude it was almost undetectable and shadowed by noise even in CW frequency measurements. For this reason, we expected FMR at 2.5 GHz to be the first step in the critical curve's evolution to high frequency.

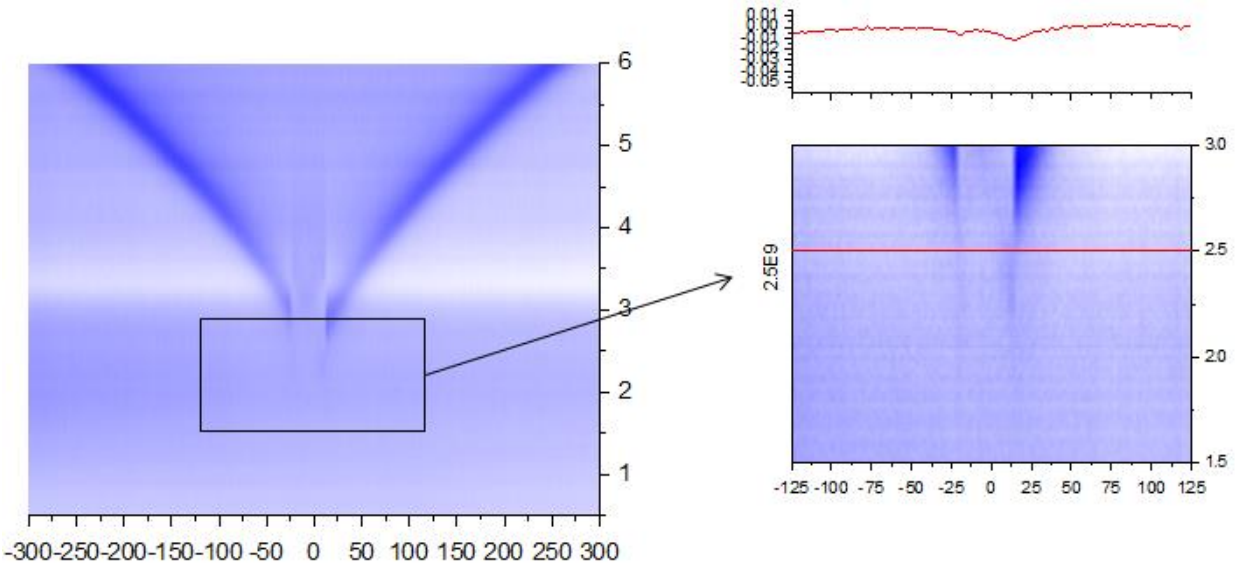

Fig. 4.1 Broadband FMR curve for R14 with a zoom in the frequency range 1.5 to 3.0 GHz.

For a better idea of how the FMR evolves from the static critical curve, the lowest CW frequency FMR is plotted along with the TDO signal at a some selected angles in Fig. 4.2 below. There exists a range of angles for which the abosorption peak of FMR matches very closely to the switching point which is indicated by the peak in the TDO signal, while at some angles more along the hard axis, the FMR signal lies just outside of the TDO curve. This evolution from low frequency to high can be better illustrated by comparing the static and dynamic critical curves, as in Fig. 4.3.

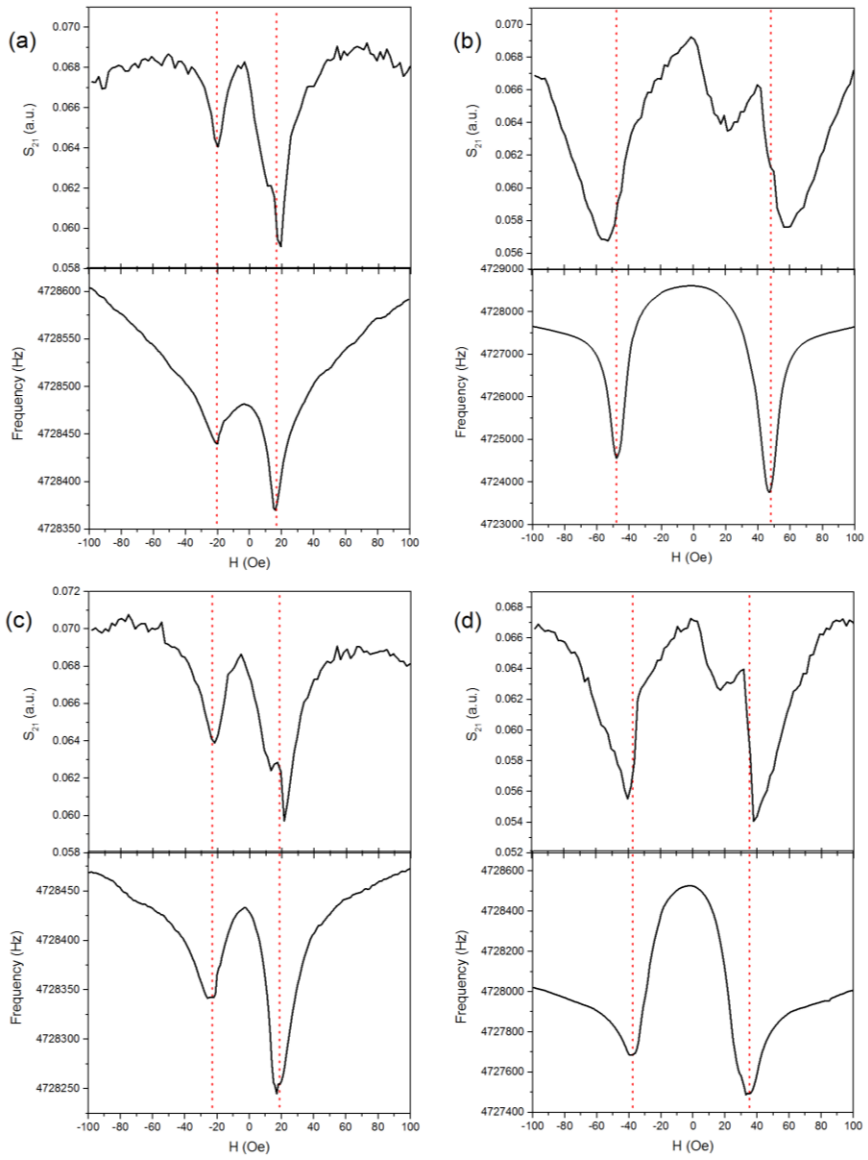

Fig. 4.2 CW FMR scans at 2.5 GHz compared to TDO signal for R16 at (a) 0° (b) 110°, (c) 150°, and (d) 300° relative to the sample's easy axis. For (a),(b),(c) and (d), *top*: FMR; *bottom*: TDO.

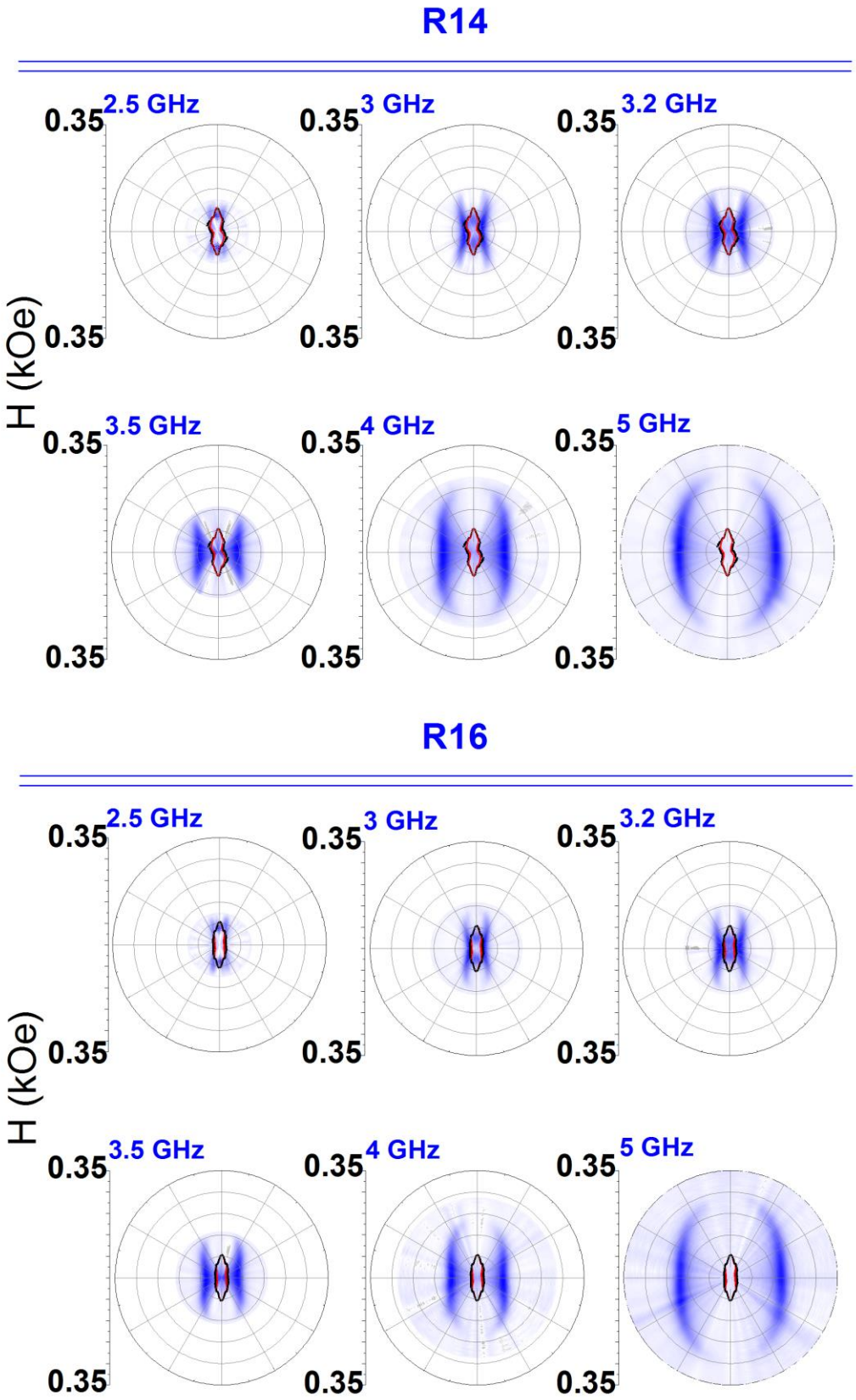

Fig. 4.3 Dynamic critical curve for both SAF samples with static switching curve superimposed.

4.3 Suggested Method for Closing the Gap

It can be immediately observed that in our polar representation of FMR, we have lost some information about the hard axis. This is to be expected, since, throughout the measurements, the hard axis is parallel to the ac magnetic field. The dc field is rotated while the ac field and sample remain fixed. FMR in general will not occur when the dc field has reached an orientation parallel to the ac field, since there will be no component of the dc field perpendicular to it. This results in a gap around the 90° and 270° directions in the dynamic polar graphs.

We suggest here a method for closing this gap. After completing the CW FMR measurements at the desired frequency around the entire 360° rotation, the sample can be turned by 90° while leaving the waveguide stationary. In this orientation, the easy axis is now parallel to the ac magnetic field. The CW FMR measurements are now repeated at the same frequency around the entire rotation. This will produce a graph in which the hard axis is well-characterized, but information about the easy axis is lost.

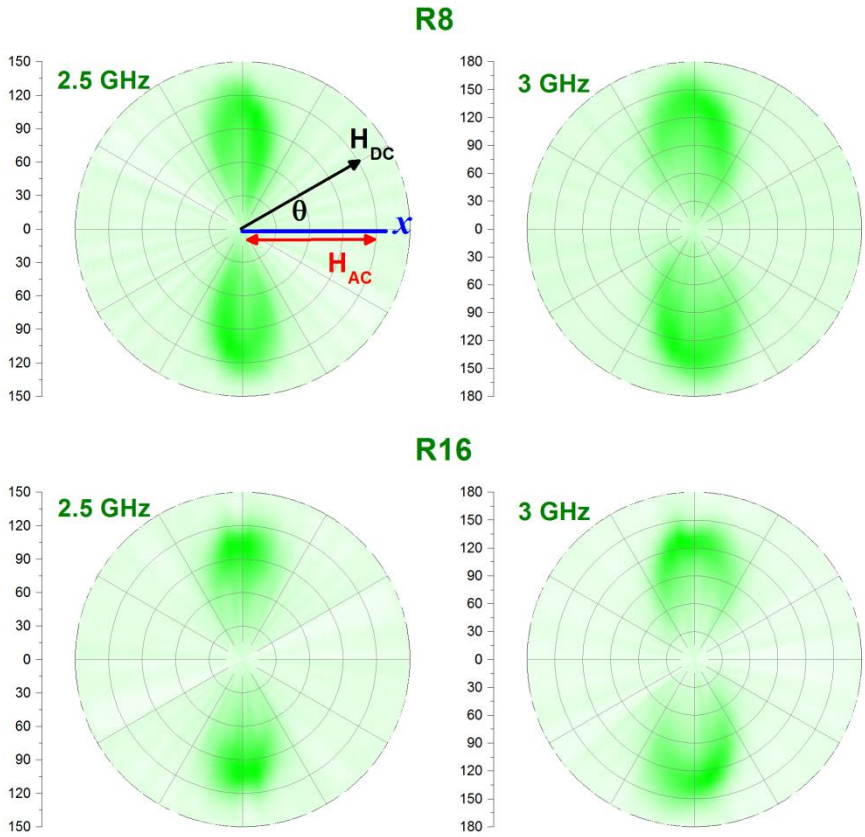

Fig. 4.4 Hard axis characterization of R8 and R16 at 2.5 GHz and 3 GHz. ***x*** is directed along the samples easy axis.

The two graphs from the different sample orientations can now be overlapped, resulting in a dynamic critical curve which contains information about any direction of the sample's magnetization. Thus, in this way, we have produced a full dynamic critical curve containing FMR information, which as we have seen is really just an extension of TS, in all directions.

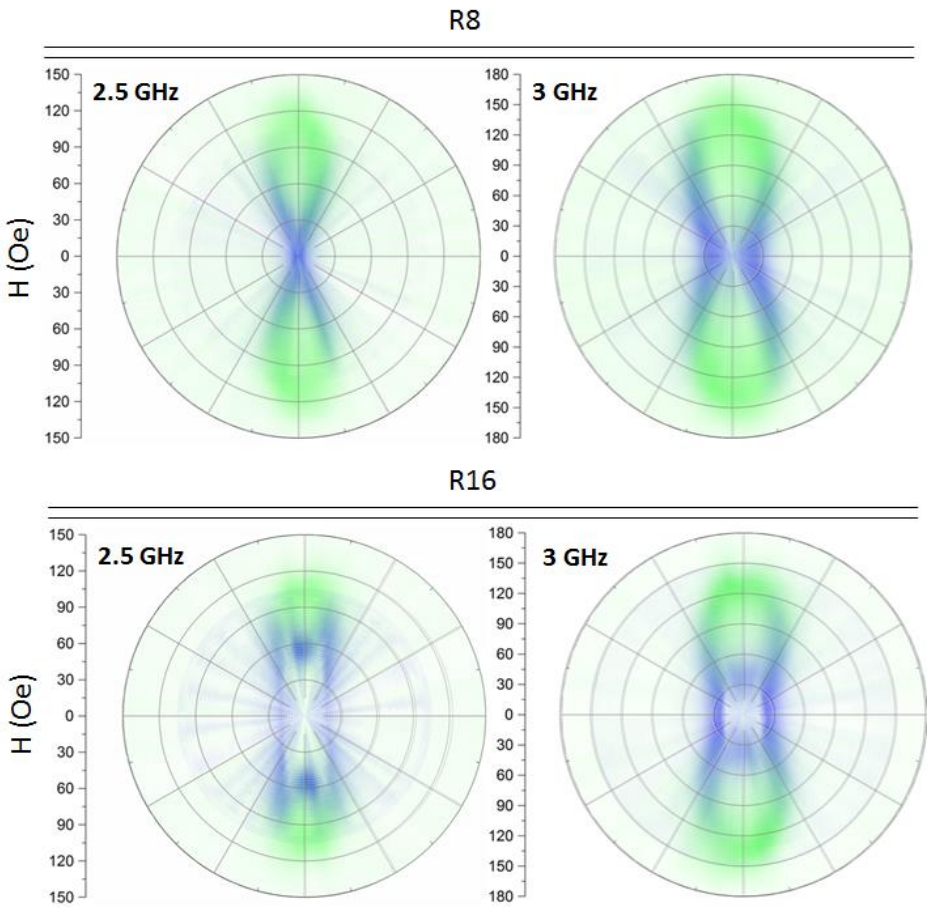

Fig. 4.5 Overlap of dynamic curves for different orientations of the selected samples.

4.4 Summary

To conclude this thesis, we have provided an elegant and concise representation of FMR for our samples, which contains complete 360° characterization in a single graph. This is a dynamic analog to the well-studied critical curve, and the anisotropy observed in the static critical curve is preserved in the dynamic. This dynamic critical curve can be done at any frequency for which the sample can be resonant, but by going to the lowest resonant frequency, this polar representation allows us to see visually that TS is the low-frequency-limit of FMR.

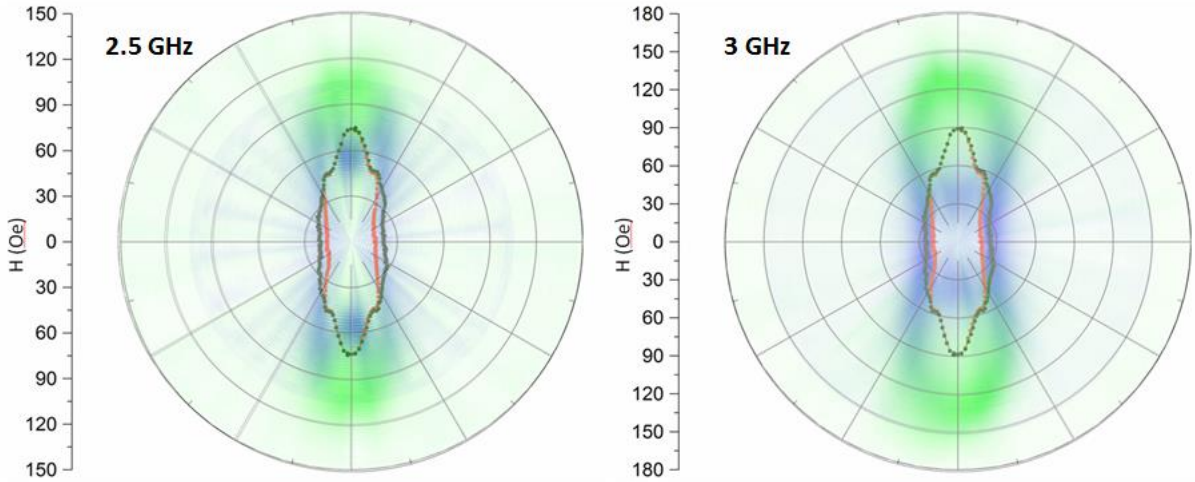

Fig. 4.6 Critical curve of R16 compared to full dynamic characterization at selected frequencies

References

1. Hirota, E.S., H.; Inomata, K., *Giant Magneto-Resistance Devices*. 2002: Springer Science & Business Media.
2. Byeon, S.C., A. Misra, and W.D. Doyle, *Synthetic antiferromagnetic soft underlayers for perpendicular recording media.* Ieee Transactions on Magnetics, 2004. **40**(4): p. 2386-2388.
3. Zhu, J.-G., *New Heights for Hard Disk Drives.* Materials Today, 2003. **6**(7-8): p. 22-31.
4. Veloso, A. and P.P. Freitas, *Spin valve sensors with synthetic free and pinned layers.* Journal of Applied Physics, 2000. **87**(9): p. 5744-5746.
5. Spinu, L., et al., *Probing two-dimensional magnetic switching in Co/SiO2 multilayers using reversible susceptibility experiments.* Applied Physics Letters, 2005. **86**(1).
6. Kittel, C., *Introduction to Solid State Physics*. 8 ed. 2005, New Jersey John Wiley & Sons.
7. Cullity, B.D., *Introduction to Magnetic Materials* 1972, New Jersey: Addison-Wiley Publishing Company.
8. Chikazumi, S., *Physics of Ferromagnetism*. 2 ed. 1997, Oxford, UK: Oxford University Press.
9. Miyazaki, T.J., Hanmin;, *The Physics of Ferromagnetism*. 2012: Springer Publishing Company
10. Trusca, O.C., et al., *Interaction Effects in Ni Nanowire Arrays.* Ieee Transactions on Magnetics, 2008. **44**(11): p. 2730-2733.
11. Nayfeh, M.H.B., Morton K., *Electricity and Magnetism*. 1985, New York: Wiley
12. Jiles, D., *Introduction to Magnetism and Magnetic Materials*. 2 ed. 1998, Florida: Taylor and Francis Group.
13. Slater, J.C., *Atomic Shielding Constants.* Physical Review, 1930. **36**.
14. Slater, J.C., *Cohesion in Monovalent Metals.* Physical Review, 1930. **35**.
15. Nolting, W.R., Anupuru *Quantum Theory of Magnetism*. 2009, Berlin: Springer.
16. Ruderman, M.A. and C. Kittel, *Indirect Exchange Coupling of Nuclear Magnetic Moments by Conduction Electrons.* Physical Review, 1954. **96**(1): p. 99-102.
17. Mahan, G.D., *Condensed Matter in a Nutshell*. 2011, United Kingdom: Princeton University Press.
18. Kasuya, T., *A Theory of Metallic Ferro- and Antiferromagnetism on Zener's Model.* Progress of Theoretical Physics, 1956. **16**(1): p. 45-57.
19. Yosida, K., *Magnetic Properties of Cu-Mn Alloys.* Physical Review, 1957. **106**(5): p. 893-898.
20. Radu, C., *Study of Magnetization Swicthing in Coupled Magnetic Nanostructured Systems*, in *Physics*. 2008, University of New Orleans.
21. Stoner, E.C.W., E. P., *A mechanism of magnetic hysteresis in heterogenous alloys.* Philosophical Transactions of the Royal Society of London, 1948. **A240**: p. 599-644.
22. Tannous, C. and J. Gieraltowski, *The Stoner-Wohlfarth model of ferromagnetism (vol 29, pg 475, 2008).* European Journal of Physics, 2009. **30**(1): p. 227-227.
23. Lenormand, D., *Characterization of Magnetic Nanostructured Materials by First Order Reversal Curve Method*, in *Physics*. 2012, University of New Orleans: New Orleans.
24. Wernsdorfer, W., et al., *Experimental evidence of the Neel-Brown model of magnetization reversal.* Physical Review Letters, 1997. **78**(9): p. 1791-1794.
25. Neel, L., *Ann. Geophys.* 1949. **5**.
26. Brown, W.F., *Thermal Fluctuations of a Single-Domain Particle.* Physical Review, 1963. **130**.
27. Bertotti, G., *Hysteresis in Magnetism: for Physicists, Materials Scientists, and Engineers*. 1998, San Diego: Academic Press.
28. *Ferromagnetic Resonance* ed. S.V. Vonsovskii. 1966, London: Paragamon Press.
29. Dorfman, Y.G., Zs. f. Phys., 1923. **17**(98).
30. Landau, L.D.L., L. M., *On the theory of the dispersion* 1935.

31. Kittel, C., Physical Review, 1947. **71**(270).
32. Polder, D., Revs. Mod. Phys., 1949. **40**(99).
33. Gilbert, T.L., Phys. Rev., 1955. **100**(1243).
34. Atherton, N.M., *Electron Spin Resonance*. 1973, Sussex, England: Ellis Horwood Limited.
35. Vittoria, C., *Microwave Properties of Magnetic Thin Films*. 1994: World Scientific Pub Co Inc.
36. Rotaru, A., et al., *Interactions and reversal-field memory in complex magnetic nanowire arrays.* Physical Review B, 2011. **84**(13).
37. Gans, R., *Zur Theorie des Ferromagnetismus: Die reversible longitudinale und transversale Permeabilitat.* Ann Phys, 1909. **29**: p. 301-315.
38. Aharoni, A.F., E. H.; Shtrikman, S.; Treves, D., *The Reversible Susceptibility Tensor of the Stoner-Wohlfarth Model* Bulletin of the Research Council of Israel, 1957. **6A**: p. 215-238.
39. Cimpoesu, D., L. Spinu, and A. Stancu, *Transverse susceptibility method in nanoparticulate magnetic media.* Journal of Nanoscience and Nanotechnology, 2008. **8**(6): p. 2731-2744.
40. Spinu, L., et al., *Vectorial mapping of exchange anisotropy in IrMn/FeCo multilayers using the reversible susceptibility tensor.* Physical Review B, 2003. **68**(22): p. 4.
41. Spinu, L., et al., *Transverse susceptibility as the low-frequency limit of ferromagnetic resonance.* Journal of Magnetism and Magnetic Materials, 2006. **296**(1): p. 1-8.
42. Clover, R.B. and W.P. Wolf, *Magnetic Susceptibility Measurements with a Tunnel Diode Oscillator.* Review of Scientific Instruments, 1970. **41**(5): p. 617-621.
43. *Electron Paramagnetic Resonance* 1972, New York: Plenum Press.
44. Pozar, D.M., *Microwave Engineering*. 4 ed. 2012: John Wiley & Sons.
45. Slonczewski, J.C., *Theory of Magnetic Hysteresis in Films and Its Application to Computers.* Ieee Transactions on Magnetics, 2009. **45**(1): p. 8-14.
46. He, H., et al., *Co/Ni (N)-Based Synthetic Antiferromagnet With Perpendicular Anisotropy and Its Application in Pseudo Spin Valves.* Ieee Transactions on Magnetics, 2010. **46**(6): p. 1327-1330.
47. Milyaev, M.A., et al., *Thermal stability of spin valves based on a synthetic antiferromagnet and Fe50Mn50 alloy.* Physics of Metals and Metallography, 2015. **116**(11): p. 1073-1079.
48. Tadisina, Z.R., et al., *Thermal stability of synthetic antiferromagnet and hard magnet coupled spin valves.* Journal of Vacuum Science & Technology A, 2008. **26**(4): p. 735-738.
49. Pietambaram, S.V., et al., *Exchange coupling control and thermal endurance of synthetic antiferromagnet structure for MRAM.* Ieee Transactions on Magnetics, 2004. **40**(4): p. 2619-2621.
50. Emley, N.C., et al., *Reduction of spin transfer by synthetic antiferromagnets.* Applied Physics Letters, 2004. **84**(21): p. 4257-4259.
51. Hernandez, S., M. Kapoor, and R.H. Victora, *Synthetic antiferromagnet for hard layer of exchange coupled composite media.* Applied Physics Letters, 2007. **90**(13): p. 3.
52. Khvalkovskiy, A.V., et al., *Basic principles of STT-MRAM cell operation in memory arrays.* Journal of Physics D-Applied Physics, 2013. **46**(7): p. 20.
53. Savtchenko, L., et al., *Method of writing to scalable magnetoresistance random access memory element*. 2003, Google Patents.
54. Radu, C., et al., *Measurement of the critical curve of a synthetic antiferromagnet.* Applied Physics Letters, 2008. **93**(2): p. 3.
55. Radu, C., et al., *Reversible susceptibility studies of magnetization switching in FeCoB synthetic antiferromagnets.* Journal of Applied Physics, 2007. **101**(9): p. 3.
56. Petrila, I. and A. Stancu, *Asymmetries influence on critical curves of the synthetic antiferromagnetic structures in magnetic random access memory.* Computational Materials Science, 2012. **51**(1): p. 122-126.

57. Kong, Y.C., S.H. Lim, and K.J. Lee, *Ferromagnetic Resonance Frequency of a Patterned Synthetic Antiferromagnet.* Journal of the Korean Physical Society, 2009. **54**(4): p. 1630-1634.
58. Gonzalez-Chavez, D.E., et al., *Interlayer coupling in spin valves studied by broadband ferromagnetic resonance.* Physical Review B, 2013. **88**(10).
59. Zhao, Z., et al., *Magnetic properties of uniaxial synthetic antiferromagnets for spin-valve applications.* Physical Review B, 2005. **71**(10): p. 104417.
60. Forrester, M., F. Kusmartsev, and E. Kovacs, *Switching dynamics of doped CoFeB trilayers and a comparison to the quasistatic approximation.* Physical Review B, 2013. **87**(17): p. 17.
61. Grünberg, P., et al., *Layered Magnetic Structures: Evidence for Antiferromagnetic Coupling of Fe Layers across Cr Interlayers.* Physical Review Letters, 1986. **57**(19): p. 2442-2445.
62. Abarra, E.N., et al., *Longitudinal magnetic recording media with thermal stabilization layers.* Applied Physics Letters, 2000. **77**(16): p. 2581-2583.
63. Fullerton, E.E., et al., *Antiferromagnetically coupled magnetic media layers for thermally stable high-density recording.* Applied Physics Letters, 2000. **77**(23): p. 3806-3808.
64. Inomata, A., et al., *Exchange coupling strength in synthetic ferrimagnetic media.* Magnetics, IEEE Transactions on, 2001. **37**(4): p. 1449-1451.
65. Maffitt, T.M., et al., *Design considerations for MRAM.* IBM J. Res. Dev., 2006. **50**(1): p. 25-39.
66. Sun, J.Z., et al., *Thermal activation-induced sweep-rate dependence of magnetic switching astroid.* Applied Physics Letters, 2001. **78**(25): p. 4004-4006.
67. Bruno, P., *Interlayer exchange coupling: a unified physical picture.* Journal of Magnetism and Magnetic Materials, 1993. **121**: p. 248-252.
68. Cimpoesu, D., et al., *Angular resonant absorption curves in magnetic nanowire arrays.* Applied Physics Letters, 2013. **102**(23): p. 5.

Vita

The author was born in Metairie, Louisiana in 1990. He received a Bachelor of Science in Physics from the University of New Orleans in 2014. He was granted a university scholarship to pursue a PhD in Engineering and Applied Science and entered the graduate program in the Department of Physics in the fall of 2014.